Nano Research
2023, 16(1): 1387–1413

ISSN 1998-0124 CN 11-5974/O4
https://doi.org/10.1007/s12274-022-4938-6

Review Article

Graphene and MXene-based porous structures for multifunctional electromagnetic interference shielding

Xi Shen[1,3] (✉) and Jang-Kyo Kim[2] (✉)

[1] *Department of Aeronautical and Aviation Engineering, The Hong Kong Polytechnic University, Hung Hom, Kowloon, Hong Kong 999077, China*
[2] *School of Mechanical and Manufacturing Engineering, University of New South Wales, Sydney, NSW 2052, Australia*
[3] *The Research Institute for Sports Science and Technology, The Hong Kong Polytechnic University, Hung Hom, Hong Kong 999077, China*

Received: 7 July 2022 / **Revised:** 17 August 2022 / **Accepted:** 18 August 2022

ABSTRACT

Electrically conductive porous structures are ideal candidates for lightweight and absorption-dominant electromagnetic interference (EMI) shielding. In this review, we summarize the recent progress in developing porous composites and structures from emerging two-dimensional (2D) graphene and MXene nanosheets for EMI shielding applications. Important properties contributing to various energy loss mechanisms are probed with a critical discussion on their correlations with EMI shielding performance. Technological approaches to constructing bulk porous structures, such as 2D porous films, three-dimensional (3D) aerogels and foams, and hydrogels, are compared to highlight important material and processing parameters required to achieve optimal microstructures. A comprehensive comparison of EMI shielding performance is also carried out to elucidate the effects of different assembly techniques and microstructures. Distinctive multifunctional applications in adaptive EMI shielding, mechanical force attenuation, thermal management, and wearable devices are introduced, underlining the importance of unique compositions and microstructures of porous composites. The process–structure–property relationships established in this review would offer valuable guidance and insights into the design of lightweight EMI shielding materials.

KEYWORDS

porous composite, graphene, MXene, electrical conductivity, electromagnetic interference (EMI) shielding

1 Introduction

Although the rapid development of consumer electronics in recent years has greatly improved the quality of life, significant electromagnetic (EM) waves are inevitably generated from them, causing signal interferences among delicate electronic components and device malfunction [1, 2]. To mitigate the EM interference (EMI), materials with high electrical conductivities such as metal films have been conventionally used as EMI shielding materials [3]. The high electrical conductivity in the order of 10^7 S·m^{-1} provides abundant charge carriers to interact with the EM field, effectively reflecting the EM waves for a high EMI shielding effectiveness (SE) of ~ 90 dB [4]. With more electronic devices becoming flexible and wearable, however, the high densities of metal films impede their applications in the next generation electronics. Moreover, the high reflection of EM waves from the metal films generates secondary EM pollution, which further deteriorates device reliability and human health [4]. Therefore, developing novel EMI shielding materials and structures with light weight, high flexibility, and absorption-dominated shielding is essential for future electronics [5].

The advancement in nanotechnology has underpinned the evolution of EMI shielding materials and structures in the past decade. In particular, the recent discoveries of novel two-dimensional (2D) materials, including graphene and MXene, bring new paradigms in the design of EMI shielding materials that can satisfy the stringent multifunctional requirements in emerging electronics [6–8]. Graphene and its derivatives, including few-layer graphene oxide (GO) and reduced graphene oxide (rGO), have been widely explored for EMI shielding applications thanks to their high electrical conductivities (of ~ 10^5 S·m^{-1} for polycrystalline graphene), large surface areas, and intrinsic flexibility [9, 10]. Most recently, a new 2D material family of transition metal carbides or nitrides—known as MXene—has been exfoliated, with many of them showing metal-like electrical conductivities [4, 11–13]. Combined with the much lower densities than metals, MXene has attracted growing attention for EMI shielding applications [2, 4, 14–17]. Nevertheless, mono- or few-layer graphene or MXene sheets exhibited limited EMI SEs of only a few dB because of the atomically thin structures [18]. To leverage the excellent electrical conductivities of graphene and MXene for practical applications, the 2D building blocks were assembled into layered structures with or without polymer binders, forming compact films with ultrahigh electrical conductivities of 10^5 to 10^6 S·m^{-1} and EMI SEs of up to 92 dB [14–16]. Despite the excellent EMI SEs achieved by compact films, the reflection of EM waves and the densities were still relatively high for lightweight and absorption-dominant EMI shielding. In addition, the films normally lacked stretchability and conformability, unsuitable for wearable EMI shielding applications. One effective strategy to improve the absorption-dominant EMI SE is the construction of multiple interfaces in the composites. Different structures, including multilayer films [19,

Address correspondence to Xi Shen, xi.shen@polyu.edu.hk; Jang-Kyo Kim, jangkyo.kim@unsw.edu.au

20], segregated networks [21], and porous structures [22], were designed to offer enhanced interfacial polarization and multiple reflection at various filler/matrix and solid/air interfaces, imparting improved absorption of EM waves and overall EMI SEs. To further reduce the density and EM reflection while improving the stretchability, myriad efforts have been made towards building porous composites and structures using graphene or MXene sheets as nanofillers [5]. Many novel techniques have been devised to achieve controlled assemblies of 2D nanofillers so as to fully translate their excellent properties into the bulk porous structures [23]. Similar 2D geometries of graphene and MXene mean that most techniques initially developed for constructing porous graphene structures can be naturally applied to MXene. The similar geometries also make it possible to construct porous structures containing hybrid fillers without modifying much of the processing parameters. Nevertheless, some distinctive differences between graphene and MXene sheets, such as functional groups and aspect ratios, warrant some fine adjustments of the processing parameters for individual fillers to achieve desired microstructures. For example, MXene sheets normally have much lower aspect ratios than graphene counterparts, necessitating the introduction of binders in many solution-based processes to ensure the interconnection between MXene sheets, which is otherwise not required in the case of large-size graphene sheets. Various porous composites in the form of porous films, aerogels or foams, and hydrogels have been developed, demonstrating promising multifunctional applications in EMI shielding for emerging wearable and portable electronics [24]. Compared to other fillers and film structures, graphene and MXene-based porous structures have several distinct advantages for multifunctional EMI shielding applications. First, the porous network of graphene and MXene segregates conductive fillers in the interconnected pore walls for a low percolation threshold and a high electrical conductivity at a low filler loading. Second, the excellent electrical and thermal conductivities of graphene and MXene make it possible to add other functionalities such as thermal management and sensing capabilities beyond simple EMI shielding, essential to meet the stringent requirements of emergent electronics with limited spaces for accommodating multiple materials. Third, porous structures possess much lower densities than solid films, ideal for lightweight EMI shielding in weight-critical applications, such as airplanes and space vehicles. Last, the absorption of EM waves can be greatly improved because of the presence of air and abundant solid/air interfaces in the porous structures, reducing the secondary EM pollution arising from the reflection. While many recent reviews have discussed the EMI shielding applications of these 2D materials, dedicated analyses on the relationship between various porous structures, including films, aerogels/foams, and hydrogels, and their EMI shielding performance, are rare [5, 24–33]. Moreover, most existing reviews focus mainly on EMI shielding performance with little scrutiny on their multifunctional applications.

Herein, this review is dedicated to synopsizing recent progress in the development of porous composites and structures from emerging 2D graphene and MXene sheets for EMI shielding applications, and its overview is schematically illustrated in Fig. 1. First, the critical properties contributing to various energy loss mechanisms, including the electrical conductivity,

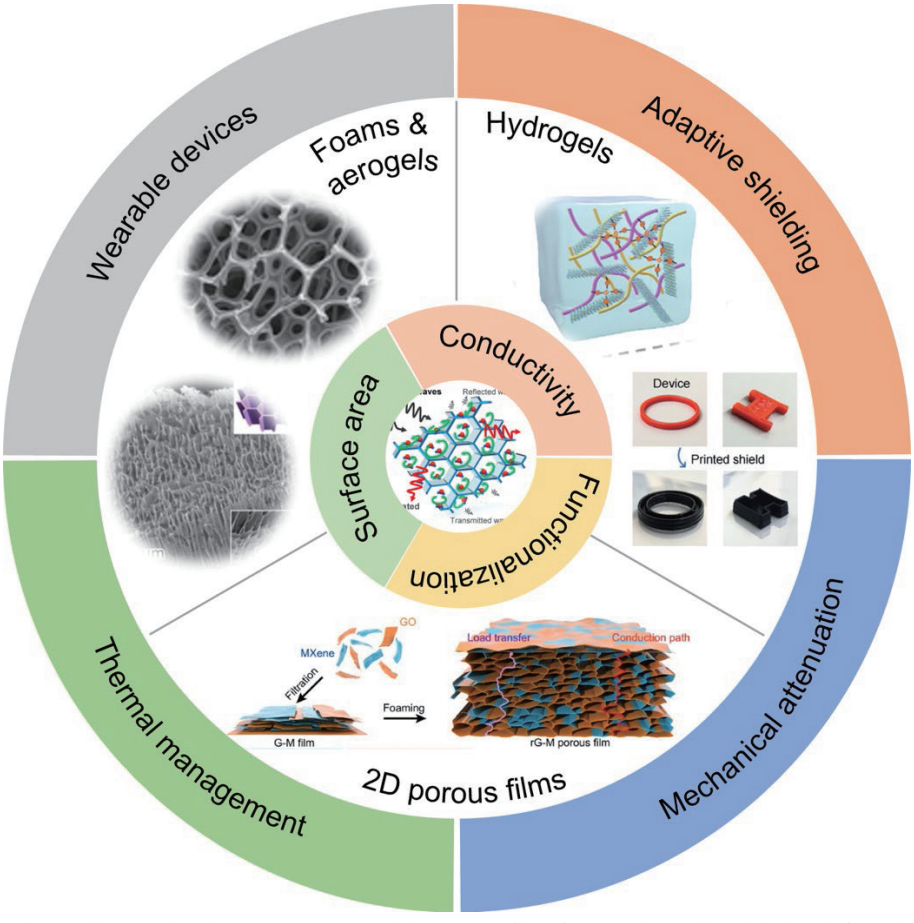

Figure 1 Overview of graphene and MXene-based porous structures including porous films, foams and aerogels, and hydrogels for multifunctional EMI shielding applications. Schematic of porous film reproduced with permission from Ref. [34], © Tsinghua University Press 2022. SEM image of graphene foam reproduced with permission from Ref. [35], © American Chemical Society 2017. SEM image of MXene aerogel reproduced from Ref. [36], © Zeng, Z. H. et al. 2020. Schematic of hydrogel reproduce from Ref. [37], © Yu, Y. H. et al. 2022. Photographs of hydrogel reproduced with permission from Ref. [38], © Wiley-VCH GmbH 2021.

functionalization, and surface area, are probed with thorough discussion on their correlation with the EMI shielding performance. Then, different assembly techniques to obtain bulk porous structures such as 2D porous films, three-dimensional (3D) aerogels or foams, and hydrogels are examined, highlighting important material and processing parameters to obtain desired microstructures and properties. Subsequently, the effects of different assembly techniques and microstructures on EMI shielding performance of different porous structures are elucidated. Finally, novel multifunctional applications in adaptive EMI shielding, mechanical force attenuation, thermal management, and wearable devices are introduced, underlining the importance of compositions and microstructures of porous composites.

2 Factors affecting EMI SE

The EMI shielding occurs through three main mechanisms, including reflection, absorption, and multiple reflection of EM waves [28]. The reflection loss is generated when the incident EM wave encounters the material surface having a vastly different impedance [27]. A high electrical conductivity offers a large impedance mismatch with air, contributing to a high reflection loss as a result of the interaction between abundant charge carriers and EM waves. The absorption loss constitutes dielectric and magnetic losses related to the permittivity and permeability of the material, respectively [31]. For graphene and MXene-based composites without magnetic fillers, the dielectric loss is the main energy loss mechanism for EM wave absorption. The dielectric loss in a conductive porous media is in turn manifested by the conduction and polarization losses. The conduction loss arises when electrical currents are generated in the conductive networks within the EM fields, converting EM energies into heat. Therefore, a high electrical conductivity is also favorable for a high conduction loss in graphene and MXene-based composites. In addition, the alternating EM field generates polarization and relaxation of various dipoles in the composites, especially at the interfaces between conductive fillers and insulating polymers, leading to polarization losses. In this connection, the interfacial interaction between conductive fillers and polymer matrix is critical to a large interfacial polarization, which is commonly modulated by creating various functional groups on graphene and MXene sheets. The last mechanism, multiple reflection, is closely related to the interaction between penetrated EM waves and internal interfaces [29]. Therefore, a large interfacial surface area with disparate impedances across the interface is conducive to multiple reflection of EM waves. In porous composites, the large interfacial surface area is provided by the abundant conductive pore wall/air interfaces, which are optimized by designing hierarchical pore structures. Based on the above mechanisms, electrical conductivity, interfaces and functional groups, and pore structures are considered as the most important material parameters determining the EMI SE. The details as to how these material parameters affect EMI SE are discussed in the following.

2.1 Electrical conductivity

The electrical conductivity affects both the reflection and absorption of EM waves. A high electrical conductivity is essential for the effective reflection of EM waves by providing abundant charge carriers to interact with the EM waves and dissipate their energies. Meanwhile, the conductive network allows the conversion of EM waves into electrical currents when the wave propagates into the material, leading to significant conduction losses in favor of a high absorption of EM waves. Owing to the intrinsically high electrical conductivities of graphene and MXene, the conduction loss is a major mechanism for EM wave absorption in a porous composite made therefrom. One effective strategy to translate the excellent electrical conductivities of graphene and MXene to porous composites is constructing a 3D percolated network. 3D graphene foams (GFs) were fabricated by chemical vapor deposition (CVD), which were further assembled into flexible porous composites by coating liquid polydimethylsiloxane (PDMS) resin onto the GFs (Fig. 2(a)) [1]. The interconnected high-quality graphene network gave rise to high electrical conductivities of GF/PDMS composites, ranging from 0.6 to 2.0 S·cm^{-1} depending on graphene loading. As shown in Fig. 2(b), the enhanced electrical conductivity directly translated into a high EMI SE to over 20 dB. Unlike the reflection-dominant EMI shielding of highly conductive metals, the excellent EMI SEs of GF/PDMS composites mainly arose from EM wave absorption thanks to the numerous pores surrounded by conductive graphene struts. The free electrons induced by the incident EM waves travelled along the conductive struts, leading to a large conduction loss and thus high absorption. The electrical conductivities of GFs were further improved by filling the large internal pores with conductive fillers or replacing the matrix with conductive polymers [35, 39, 40]. For example, poly(3,4-ethylenedioxythiophene):poly(styrene sulfonate) (PEDOT:PSS) was used as the conductive matrix in a GF/PEDOT:PSS composite by coating PEDOT:PSS solution on the CVD-grown GF (Fig. 2(c)) [35]. The scanning electron microscopy (SEM) images clearly indicate that the graphene struts were almost completely connected by the conductive PEDOT:PSS, providing additional conductive pathways for a much-improved electrical conductivity over 40 S·cm^{-1}. As a result, an exceptional EMI SE of over 90 dB was attained by the GF/PEDOT:PSS composite. This value is comparable to those of conventional metals, such as copper foils [41], but was achieved at a much lower density of only 0.076 g·cm^{-3} in the GF/PEDOT:PSS composite. In addition to graphene, MXene of different elemental compositions also exhibited superior electrical conductivities [25]. Amongst different MXenes, $Ti_3C_2T_x$ showed the highest electrical conductivity of over 8,500 S·cm^{-1} [25], making it the most widely investigated MXene for EMI shielding. Although $Ti_3C_2T_x$ nanosheets cannot be assembled into 3D structures by template-directed CVD, other techniques such as foaming and ice-templating have been developed to construct $Ti_3C_2T_x$ MXene-based foams and aerogels [27]. Thanks to the intrinsically high electrical conductivities of $Ti_3C_2T_x$ nanosheets and interconnected networks, the electrical conductivity of the $Ti_3C_2T_x$ foam reached as high as 500 S·cm^{-1} with an EMI SE of 70 dB [16].

2.2 Interface and functional group

In addition to the conduction loss caused by a high electrical conductivity, another important mechanism contributing to high EM wave absorption is the polarization relaxation [30]. There are two main types, namely dipole and interfacial polarization, both of which can be achieved by introducing functional groups on the conductive fillers [42–45]. Electric dipoles exist between polar functional groups with high electronegativities and anchoring atoms. The electric dipole moments can be induced or removed under alternating EM fields, inducing significant energy losses to the incident EM waves. Common oxygenated functional groups, including hydroxyl, epoxide, and carboxyl groups, were generated on the surface of GO and rGO, serving as sources of dipole polarization [42–44]. However, excessive functional groups were not preferred because they significantly impaired the intrinsically high electrical conductivity of graphene, potentially reducing the conduction losses and in turn adversely affecting the EMI SE. On the contrary, polar functional groups created on MXene

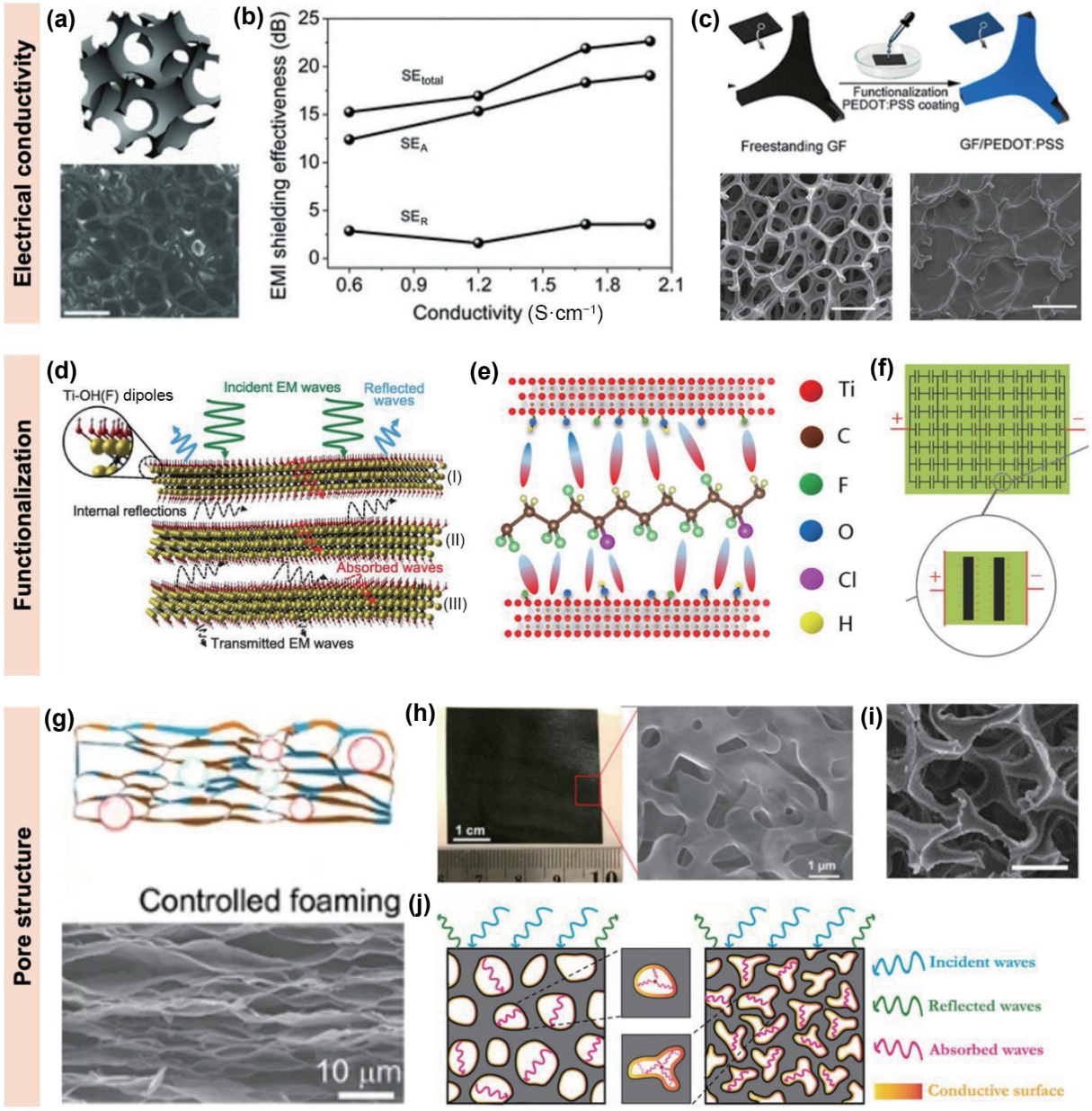

Figure 2 Key factors affecting the EMI SEs of porous composites. (a) Schematic and SEM image of GF (scale bar: 500 μm). (b) Effect of electrical conductivity on reflection (SE_R), absorption (SE_A), and overall EMI SE (SE_{total}). Reproduced with permission from Ref. [1], © WILEY-VCH Verlag GmbH & Co. KGaA, Weinheim 2013. (c) Schematics of the fabrication of GF/PEDOT:PSS composite and SEM images of the porous composites before and after PEDOT:PSS coating (scale bars: 500 μm). Reproduced with permission from Ref. [35], © American Chemical Society 2017. Schematics of (d) dipole polarization, (e) interfacial polarization, and (f) formation of micro-capacitors owing to functionalization. (d) Reproduced with permission from Ref. [4], © American Association for the Advancement of Science 2016. (e) Reproduced with permission from Ref. [45], © American Chemical Society 2018. (f) Reproduced with permission from Ref. [2], © WILEY-VCH Verlag GmbH & Co. KGaA, Weinheim 2014. (g) Schematic and SEM image of the porous rGO-MXene film made by a foaming process. Reproduced with permission from Ref. [34], © Tsinghua University Press 2022. (h) Optical and SEM images of porous graphene film with nanoscale pores. Reproduced with permission from Ref. [54], © Elsevier Inc. 2019. (i) SEM image of the MXene/PU foam (scale bar: 200 μm). (j) Schematic showing the mechanisms of EMI shielding of auxetic (right) and non-auxetic (left) structures. Reproduced with permission from Ref. [55], © Elsevier Ltd. 2021.

nanosheets during the synthesis brought about dipole polarization without compromising their high electrical conductivity [4]. As shown in Fig. 2(d), the electronegative functional groups, especially fluorine groups, formed dipoles with the Ti atoms in $Ti_3C_2T_x$, which were polarized and relaxed under alternating EM fields to dissipate the EM energy. This work confirmed the dipole polarization as an important additional shielding mechanism in MXene-based materials besides the conduction loss, leading to superior EMI SE than graphene-based counterparts.

Interfacial polarization is also an important mechanism in polymer composites because of the presence of numerous filler/matrix interfaces [35]. The contrasting dielectric properties between electrically conductive fillers and insulating matrix allowed the accumulation and redistribution of charges at their interfaces under EM fields according to the Maxell–Wagner–Sillar (MWS) effect, giving rise to interfacial polarization [46]. The interfacial polarization can be enhanced through forming local dipoles at the interfaces by means of functionalization, as shown in Fig. 2(e). The functional groups, such as hydroxyl and fluorine species, on the surfaces of $Ti_3C_2T_x$ nanosheets formed polar hydrogen bonds with polyvinylidene difluoride (PVDF) chains to create nanoscale dipoles at the interfaces which could be polarized and relaxed under alternating EM fields [45]. In addition to $Ti_3C_2T_x$, GO or rGO sheets also formed hydrogen bonds with various polymer matrices to facilitate interfacial polarization because of the abundant oxygenated functional groups on them

[47, 48]. The interfacial polarization created numerous nano- and micro-capacitors consisting of conductive electrodes surrounded by insulating polymers in the polymer composites (Fig. 2(f)), leading to improved dielectric constant for polarization losses [2].

The dipole and interfacial polarizations are common for composites containing GO, rGO, and MXene sheets. As noted above, the introduction of functional groups in graphene reduced the intrinsic electrical conductivity [49], deleterious to high conduction losses. On the other hand, pristine graphene made by CVD showed excellent conduction losses, but unable to facilitate polarization losses due to the lack of polar functional groups [50]. This means that only one mechanism, either polarization or conduction loss, prevails in graphene-based composites depending on the degree of functionalization. By contrast, the simultaneous polarization and conduction losses in MXene-based composites lead to generally higher EMI SEs than rGO or graphene-based counterparts.

2.3 Pore structure

One unique mechanism contributing to EMI shielding in porous structures is the multiple internal reflection of EM waves [51]. The penetrating EM waves interact with the conductive cell walls and are reflected multiple times at the air/cell wall interfaces where the impedance mismatch prevails, dissipating their energy and thus manifesting high absorption of EM waves. Because a large surface area is desired to provide sufficient interfaces for multiple reflection, several methods have been used to expand the surface area by creating pores in 2D films and 3D structures with controlled sizes and morphologies. Highly porous graphene or MXene films were made by a foaming process from the compact films, as shown in Fig. 2(g) [34]. The compact film was placed between two glass slides with a copper foil as the spacer and wetted by hydrazine serving as the foaming agent. The hydrazine reacted with oxygen containing functional groups on rGO or $Ti_3C_2T_x$ sheets to form gases such as CO_2 and CO. The processing conditions for the rGO-$Ti_3C_2T_x$ hybrid films were optimized by tuning the mass ratio of rGO to $Ti_3C_2T_x$ for controlling the amount of gases generated. The gases generated during the foaming process expanded the interlayer spacing to achieve elongated pores with sizes of several microns, which enabled internal reflection of EM waves for high absorption. The porous film made from rGO-$Ti_3C_2T_x$ hybrids by the foaming process exhibited an EMI SE of 42.5 dB at a thickness of 50 μm and a density of 0.26 g·cm^{-3}, giving rise to an excellent specific SE (SSE) per thickness (t), SSE/t, of over 33,000 dB·cm^2·g^{-1} thanks to the highly porous structure [34]. Nevertheless, the pore sizes in these porous films were still of micrometer scale, too large to form dense conductive networks and sufficient surface areas for EM wave attenuation [52]. Further enhancing the SSE/t was possible by reducing the pore size to a nanometer range [53, 54]. A porous graphene film with pore sizes of only hundreds of nanometers was prepared by CVD on a de-alloyed Ni film, as shown in Fig. 2(h) [54]. The nanoscale pores gave rise to huge specific surface areas of up to 1,260 m^2·g^{-1}, offering excellent EMI absorption through multiple internal reflection. Combined with a thickness of 35 μm and a density of 0.049 g·cm^{-3}, an exceptional SSE/t value of over 100,000 dB·cm^2·g^{-1} was attained by the nano-porous graphene film, much superior to its counterparts having micron-sized pores. In addition to pore size, the pore morphology can also be tuned to avail a large surface area. The auxetic MXene- [55] and rGO-based [56] polymer foams have been used for EMI shielding by virtue of their larger surface areas than the non-auxetic structures. The reentrant structure comprising buckled struts in the auxetic MXene/polyurethane (PU) foam (Fig. 2(i)) offered a 32% larger conductive surface area than its non-auxetic counterpart of the same density, providing more interfaces for scattering the incident EM waves (Fig. 2(j)) and thus higher absorption [55].

3 Rational assemblies of porous structures

3.1 2D porous films

Thin metal foils are conventional EMI shielding materials but suffer from high densities and susceptibility to corrosion. Compact films made from conductive 2D graphene and MXene show good EMI SEs thanks to their excellent electrical conductivity and layered structures [4, 15]. Creating pores in the films can further improve the absorption through increasing the surface area for enhanced multiple reflection while reducing the density [57]. Nonetheless, the existence of pores may compromise the electrical conductivity and mechanical properties of the films. Therefore, it is of paramount importance to carefully regulate the microstructures of pores and pore walls to enhance the surface area while minimizing the potentially adverse impact on electrical and mechanical properties. To this end, several rational assembly techniques have been developed, including the sacrificial templating and modified self-assembly.

Sacrificial templating. Polymer spheres are common sacrificial templates to guide the assembly of 2D graphene or MXene nanosheets [23]. Common templates include poly(methyl methacrylate) (PMMA) and polystyrene (PS) spheres which boast their strong interactions with rGO and MXene sheets and can be easily removed by thermal treatments [58]. A $Ti_3C_2T_x$ film was fabricated by a vacuum filtration method with PMMA spheres as templates, as shown in Fig. 3(a) [59]. The $Ti_3C_2T_x$ sheets wrapped around the PMMA spheres during the infiltration process owing to the strong interaction between their surface functional groups, forming interconnected hollow spheres with $Ti_3C_2T_x$ walls after removing PMMA by annealing at 450 °C (Fig. 3(b)). The $Ti_3C_2T_x$ walls of two adjacent spheres were in firm contact through hydrogen or van der Waals (vdW) bonds (Fig. 3(c)), offering interconnected conductive networks throughout the whole film and thus an excellent electrical conductivity of 200 S·cm^{-1}. Although this value was lower than the compact $Ti_3C_2T_x$ film [4, 49], it was much superior to those of 3D graphene and MXene foams or aerogels (ranging from 10 to 50 S·cm^{-1}) [50, 58]. As such, porous rGO and MXene films were fabricated using PS or PMMA spheres as templates for EMI shielding applications [60–62]. Several parameters, such as annealing temperature and sphere size, were found important for overall EMI SEs of porous films. First, the annealing temperature used to remove the polymer templates was vital to the integrity of porous structure and the resulting electrical conductivity, especially for rGO-based porous films. With increasing temperature, GO was *in-situ* reduced to rGO during the removal of PS spheres [60]. However, a temperature higher than 1,000 °C resulted in a drop in electrical conductivity of porous rGO film because of the collapsed porous structure at high temperatures. Therefore, the thermal annealing at an optimized temperature of 800 °C led to the highest EMI SE of 42 dB, over 30% higher than that annealed at 1,200 °C, for rGO porous films. Second, the size of polymer spheres determined the pore size and thus the electrical conductivity. The larger was the PMMA spheres the larger was the pore size in the $Ti_3C_2T_x$ film, leading to lower electrical conductivities and smaller surface areas than those made from smaller spheres [62]. Therefore, the $Ti_3C_2T_x$ films made from smaller PMMA spheres showed higher absorption and EMI SEs than the ones made from large spheres. Overall, the porous films showed significantly higher EMI SEs than their nonporous counterparts, mainly because of much improved absorption arising from the porous structures with a

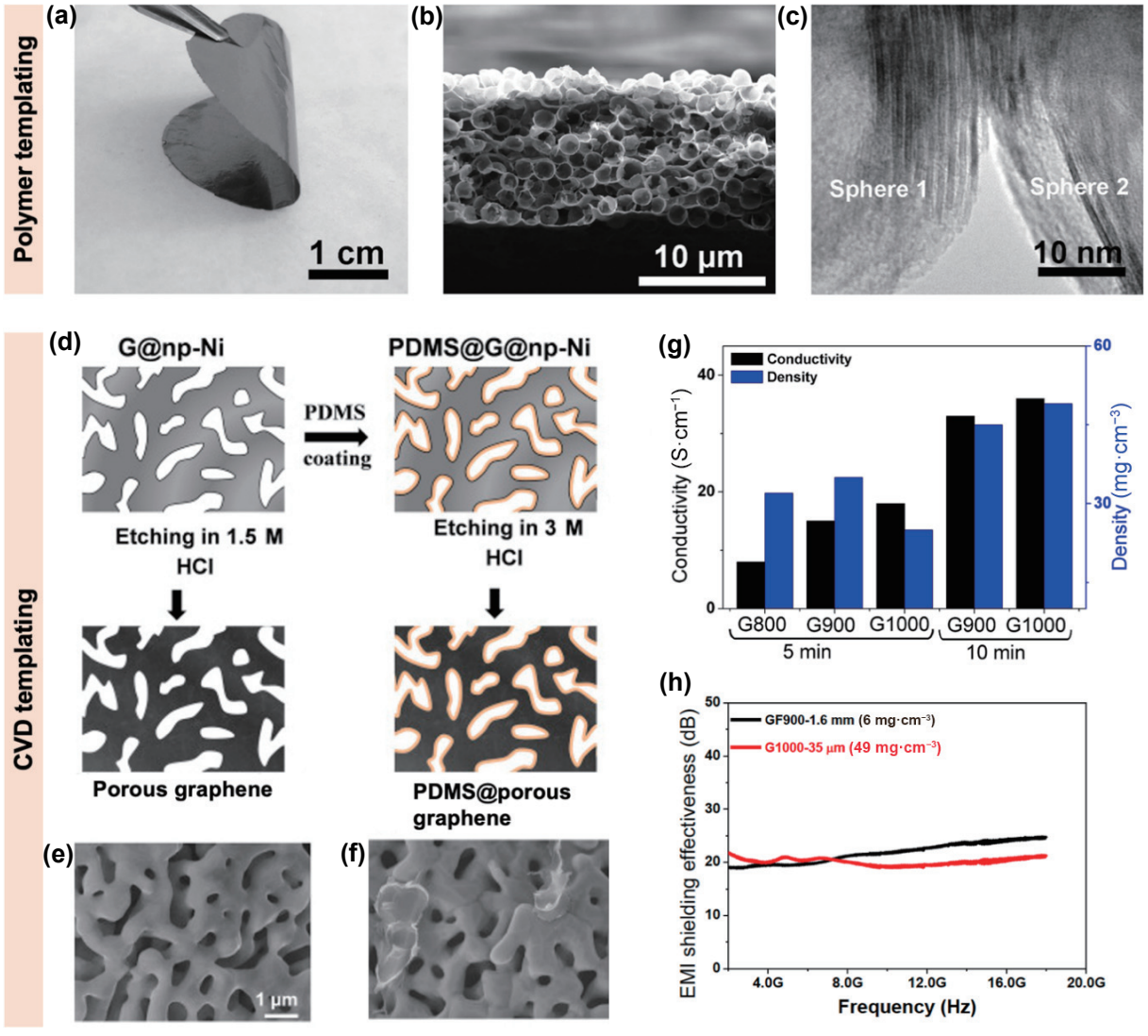

Figure 3 Fabrication of porous 2D films with nanoscale pores by sacrificial templating. (a) Optical, (b) cross-sectional SEM, and (c) TEM images of $Ti_3C_2T_x$ film fabricated by vacuum infiltration method using PMMA spheres as templates. Reproduced with permission from Ref. [59], © WILEY-VCH Verlag GmbH & Co. KGaA, Weinheim 2017. (d) Schematics of the fabrication of porous graphene films on de-alloyed Ni templates. SEM images of (e) porous graphene and (f) PDMS@porous graphene films. (g) Electrical conductivities and densities of porous graphene films prepared at different growth temperatures and times. (h) EMI SEs of porous graphene film and GF. Reproduced with permission from Ref. [54], © Elsevier Inc. 2019.

minimum reduction in electrical conductivity.

The polymer sphere templates normally had sizes larger than 1 μm, translating into micrometer-sized pores in the porous film. Further reducing the pore size to nanometer ranges is desired to provide more conductive networks and larger specific surface areas, which requires templates featuring nanoscale sizes [53]. A Ni film with nanosized pores synthesized by dealloying was used as the sacrificial template to fabricate a graphene film by template-directed CVD, as shown in Fig. 3(d) [54]. A freestanding graphene film having pores of sizes less than 1 μm was obtained after etching the Ni template using HCl solution (Fig. 3(e)). Alternatively, PDMS coating was applied before etching to yield PDMS@porous graphene composites with better mechanical flexibility and stretchability (Fig. 3(f)). The growth temperature and time of graphene were important parameters in determining the surface area and electrical conductivity of the porous film. As shown in Fig. 3(g), increasing the growth temperature from 800 to 1,000 °C led to more than one-fold improvement in electrical conductivity to 18 S·cm^{-1} owing to the reduced defects in graphene [63]. Higher densities were achieved with longer growth time [64], further doubling the electrical conductivity to 36 S·cm^{-1}. Despite the increased pore sizes at higher growth temperatures and longer growth time, a large surface area of ~ 1,000 m^2·g^{-1} was still achieved because of the nano-sized pores. The combination of high electrical conductivity and large surface area in the graphene film with nanoscale pores was responsible for a high EMI SE of 18.5 dB at a thickness of only 35 μm, comparable to that attained by a much thicker GF at 1.6 mm (Fig. 3(h)). A further increase of thickness to 300 μm brought about an exceptional SE of 83 dB, corresponding to an SSE/t value of over 61,000 dB·cm^2·g^{-1} thanks to its low density of 0.045 g·cm^{-3}. The SSE/t value was superior to many MXene and graphene-based films and foams [1, 15, 16]. Despite the potential of fabricating high-quality graphene, the success of CVD templating in producing graphene films with nanoscale pores depended largely on the availability of de-alloyed templates. Moreover, the CVD process cannot be used to produce MXene films with nano-sized pores [52]. Other porous templates, such as polyethylene (PE) films containing nanoscale pores, were attractive for low-cost production of MXene films by simple spray-coating for EMI shielding applications [65].

Self-assembly. In addition to the template-directed assemblies, 2D graphene and MXene sheets can self-assemble into layered films having porous structures with proper treatments during or after the infiltration process. GO and MXene sheets are known to self-assemble into compact films with highly aligned structures by vacuum filtration driven by the strong face-to-face interaction

between the 2D sheets [49, 66]. To create pores in the self-assembled films, either ion/polymer spacers [67–69] or post-assembly freeze-drying techniques [70] were used to mitigate the interlayer stacking. In particular, cations such as Ca^{2+} and NH_4^+ were found effective in guiding the assembly of 2D sheets into porous structures by forming locally crosslinked networks with the negatively charged functional groups [71, 72]. As shown in Fig. 4(a), ammonium bicarbonate (NH_4HCO_3) was added into the GO and $Ti_3C_2T_x$ mixture solution where NH_4^+ ions interacted with negatively charged –COOH groups at the edges of GO sheets, forming 3D networks of GO and $Ti_3C_2T_x$ sheets during infiltration to yield a porous $Ti_3C_2T_x$/rGO film after reduction [73]. The SEM images show porous cross-sections of the hybrid film with thick walls consisting of stacked rGO and $Ti_3C_2T_x$ sheets (Fig. 4(b)). Although the hybrid film had a lower electrical conductivity than the $Ti_3C_2T_x$ film (Fig. 4(c)), the former delivered a higher EMI SE of 60 dB than the latter (Fig. 4(d)) because of its porous structure which was not attainable in the compact $Ti_3C_2T_x$ film.

The ion-induced self-assembly was effective in creating pores by large-size GO sheets, but was unable to prevent restacking of $Ti_3C_2T_x$ sheets with small lateral dimensions and limited flexibility. For the $Ti_3C_2T_x$ films, post-filtration processes are necessary to introduce ample pores. Hydrazine was used as the foaming agent which reacted with functional groups on $Ti_3C_2T_x$ sheets similar to the reduction process of GO films [74], expanding the as-prepared $Ti_3C_2T_x$ film into a porous structure [16]. The pore size and structure were further optimized by mixing GO and $Ti_3C_2T_x$ nanosheets so as to control the surface chemistries, as shown in Fig. 4(e) [34]. Compared to the rGO film with an enlarged thickness of 100 μm and large pores of more than 10 μm in size, the rGO-$Ti_3C_2T_x$ (rG-M) hybrid film showed a rather modest thickness increment to 60 μm and much smaller pore sizes (Fig. 4(f)). The addition of $Ti_3C_2T_x$ nanosheets reduced the amount of active functional groups which could react with hydrazine, generating a less amount of gases for a milder foaming

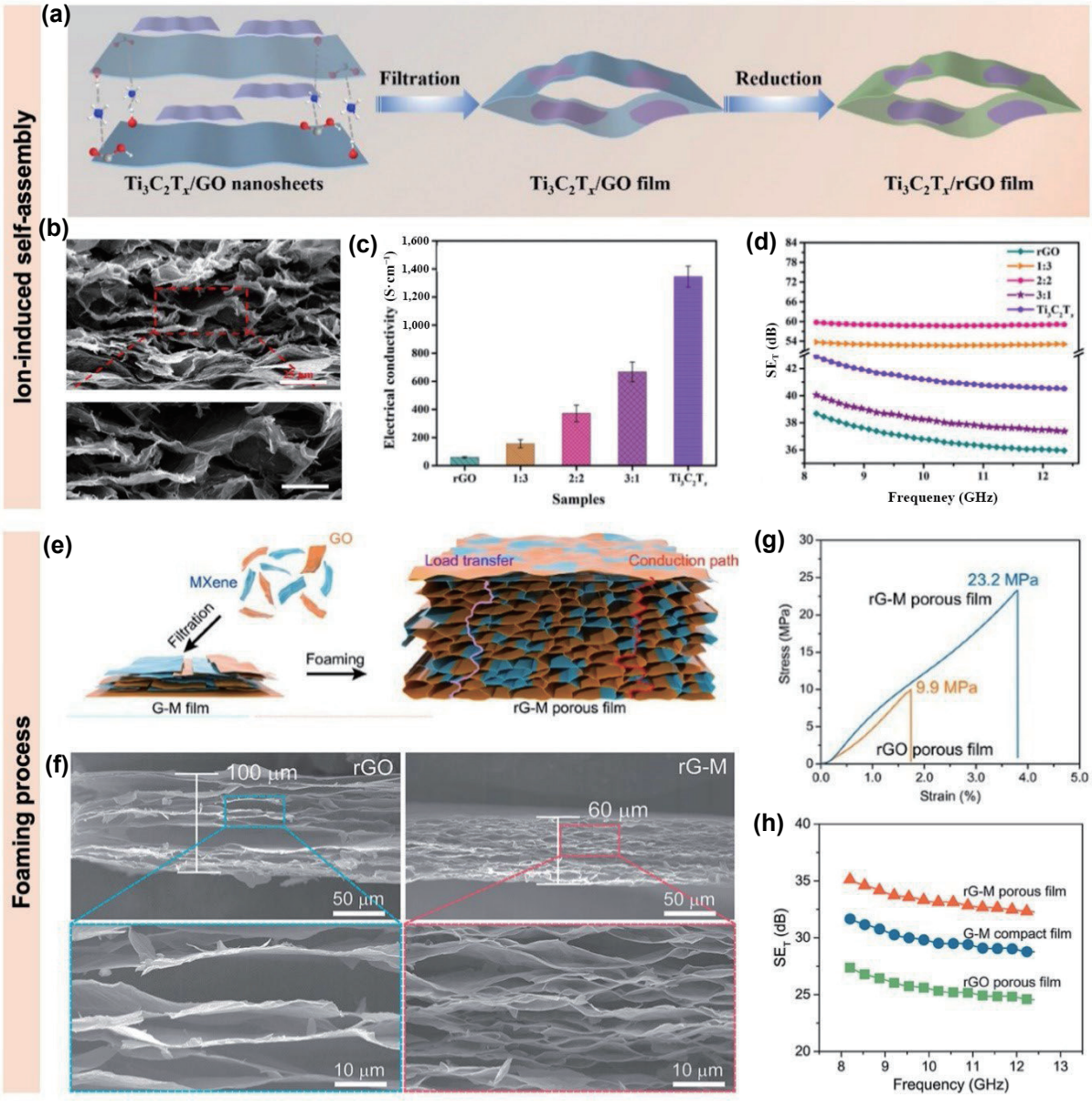

Figure 4 Fabrication of porous films by self-assembly. (a) Schematics of the NH_4^+ induced self-assembly of porous $Ti_3C_2T_x$/rGO hybrid films. (b) Cross-sectional SEM images of the $Ti_3C_2T_x$/rGO film. Scale bars: 25 μm (top) and 15 μm (bottom). (c) Electrical conductivities and (d) EMI SEs of the hybrid films with different $Ti_3C_2T_x$ to rGO ratios. Reproduced with permission from Ref. [73], © Elsevier Ltd. 2020. (e) Schematics of hydrazine induced foaming of rG-M porous films. (f) Cross-sectional SEM images of the rGO and rG-M films made by hydrazine-induced foaming. (g) Stress–strain curves and (h) EMI SEs of rGO and rG-M films. Reproduced with permission from Ref. [34], © Tsinghua University Press 2022.

process. Such smaller pore sizes were conducive to a larger surface area and better interconnected cell walls in the rG-M film, giving rise to a high strength of 23.2 MPa, more than double the rGO film (Fig. 4(g)), as well as twice higher EMI SE than the rGO film (Fig. 4(h)). In addition to chemical foaming, thermally-induced foaming processes using laser [75, 76] or sunlight [77] were also employed to create porous films. Compared to the ion-induced self-assembly during infiltration, these foaming processes can better control the pore size and morphology despite the need of additional steps after the infiltration [78].

3.2 3D foams and aerogels

Apart from film-based EMI shielding materials with thicknesses ranging from tens to hundreds of micrometers, 3D porous foams and aerogels are also common forms widely used in mission-critical electronics for aerospace and military applications because of their low densities [24]. Constructing graphene and MXene into porous foams and aerogels is particularly conducive to exploiting their excellent electrical conductivities for light-weight EMI shielding applications. Several different assembly methods, such as dip coating, template-directed CVD, and freeze-casting, have been devised to tailor the electrical conductivity, surface area, and the functionalization of graphene and MXene-based foams for boosted EMI SEs. The characteristics and relative merits of these approaches are discussed as follows.

Dip coating. Dip coating of graphene and MXene solutions onto the skeletons of polymer foams is a facile and straightforward approach to construct conductive foams for EMI shielding. One of the major benefits of dip coating is that because the pore morphology is a replica of the foam template, it can be readily tweaked before the coating to achieve desired microstructures. For example, the original PU (OPU) foam was triaxially compressed to create an auxetic PU (APU) foam which served as the template in the subsequent dip coating of $Ti_3C_2T_x$ solution, as shown in Fig. 5(a) [55]. Compared to the non-auxetic PU (NAPU) foam with straight skeletons, the APU with a similar density comprised buckled struts resulting from the triaxial compression (Fig. 5(b)). The buckled skeletons not only yielded a reentrant structure for a negative Poisson's ratio but also a larger surface area of APU than NAPU. Therefore, the MXene (MX)/APU foam absorbed more efficiently the EM waves despite similar EM reflection performance given the almost identical electrical conductivity when compared to the MX/NAPU foam (Figs. 5(c) and 5(d)), ultimately leading to a 31% higher total EMI SE than its non-auxetic counterpart (Fig. 5(d)). Similar approaches to controlling pore morphologies using auxetic structures have also been applied to graphene and hybrid fillers for improved surface areas in the dip-coating process [56, 79].

Another advantage of the dip-coating technique lies in its suitability for large-scale fabrication owing to the wide availability of polymer foams and simple coating process. As shown in Fig. 5(e), a $Ti_3C_2T_x$-coated polyimide (PI) composite foam was made by dip coating followed by chemical crosslinking, exhibiting large lateral dimensions of 60 cm × 60 cm and excellent flexibility (Fig. 5(f)) [80]. The electrical conductivity and EMI SE of the composite foam could be simply tailored by the number of coating cycles. More coating cycles meant higher electrical conductivities and higher densities as a consequence of increased $Ti_3C_2T_x$ loading (Fig. 5(g)), translating into amplified EMI SEs mainly because of the higher absorption through the interactions of EM waves with conductive walls (Fig. 5(h)). As shown in Fig. 5(i), the experimental SEs were much higher than the theoretical values (labeled as "Th-SE") calculated for homogeneous shielding materials, indicating a pivotal contribution of pores to SE improvement. In sum, dip coating is a simple and effective method to coat conductive layers on common polymer foam templates, including melamine, PI, and PU foams, taking advantage of their open cell structure and high porosity for lightweight EMI shielding applications [81–84].

Template-directed CVD. The CVD method has been developed to fabricate high-quality mono- to few-layer graphene sheets with few defects [85], which are ideal building blocks for 3D graphene structures with high electrical conductivities [86]. The growth of graphene on a porous Ni foam template by CVD has been extensively employed to fabricate GFs comprising interconnected struts and highly conductive 3D structures for EMI shielding applications [64]. Several strategies have been proposed to improve their electrical conductivity and surface area. For example, other conductive fillers or polymers, such as carbon nanotubes (CNTs) [39], metal oxide nanoparticles [40], Mxene [87], and PEDOT:PSS [35], were integrated into the GF structure to yield hybrids. The most common method was to coat the freestanding GF with conductive fillers or polymers, as shown in Fig. 6(a) [35]. The pristine GF before coating contained large and open pores with clear grain boundaries on the skeleton surface (Fig. 6(b)), whereas the pores were filled and their openings were blocked after coating with PEDOT:PSS (Fig. 6(c)). This observation signifies that the highly conductive PEDOT:PSS coating not only covered the skeleton surfaces, but also connected the large and open pores in between, contributing to more than three-fold enhancement in electrical conductivity of the GF/PEDOT:PSS composites (Fig. 6(d)). The excellent electrical conductivity of 43 $S \cdot cm^{-1}$ recorded at a PEDOT:PSS to GF mass ratio of 7 was mainly responsible for the composite's exceptional EMI SE of 92 dB.

While coating is a simple way to integrate secondary fillers with GFs, strong bonds between them cannot be guaranteed while the porosity can also be reduced when the fillers fill up the pores. To address the issues, secondary structures, such as CNTs, metal oxides, and carbon nanowires (CNWs), were grown directly onto the graphene skeleton to create a hierarchical structure [40, 88, 89]. For example, CNWs were grown on the GF structs using acetone as the liquid carbon source and cobalt nanoparticles as the catalyst, delivering a hierarchical structure across multiple length scales (Fig. 6(e)) [88]. The SEM and transmission electron microscopy (TEM) images of the CNWs/GF confirmed the uniform distribution of CNWs grown on GF struts and the formation of covalent bonds at their interfaces while the original GF's porous structure was kept intact (Fig. 6(f)). These findings contrasted with the CNTs directly deposited onto the GF by dip coating, where the open pores were filled by CNTs and there were only weak vdW forces between CNTs and GF. Consequently, the hierarchical CNWs/GF achieved an EMI SE of 36 dB (Fig. 6(g)), 38% higher than that of the CNTs/GF by dip coating (Fig. 6(h)), because of the higher absorption of EM waves by the former structure. Compared to the 3D foams made by dip coating where solution-based GO or rGO is commonly used as the building blocks, the high-quality graphene by CVD offers much higher electrical conductivities of GFs. However, the cost and scalability of template-directed CVD are less attractive than the simple dip-coating technique.

Freeze-casting. The freeze-casting technique utilizes the growing ice crystals as templates to realize ordered 3D structures from 2D graphene or MXene nanosheets dispersed in a aqueous solution [90]. The most unique feature of freeze-cast structures is the highly anisotropic pores created by the directional growth of ice crystals [91, 92]. Various freeze-casting techniques have been developed to rationally control the alignment of 2D nanosheets and the directional pores [43, 44, 46, 93–97]. Depending on the ice growth directions, they can be classified into unidirectional,

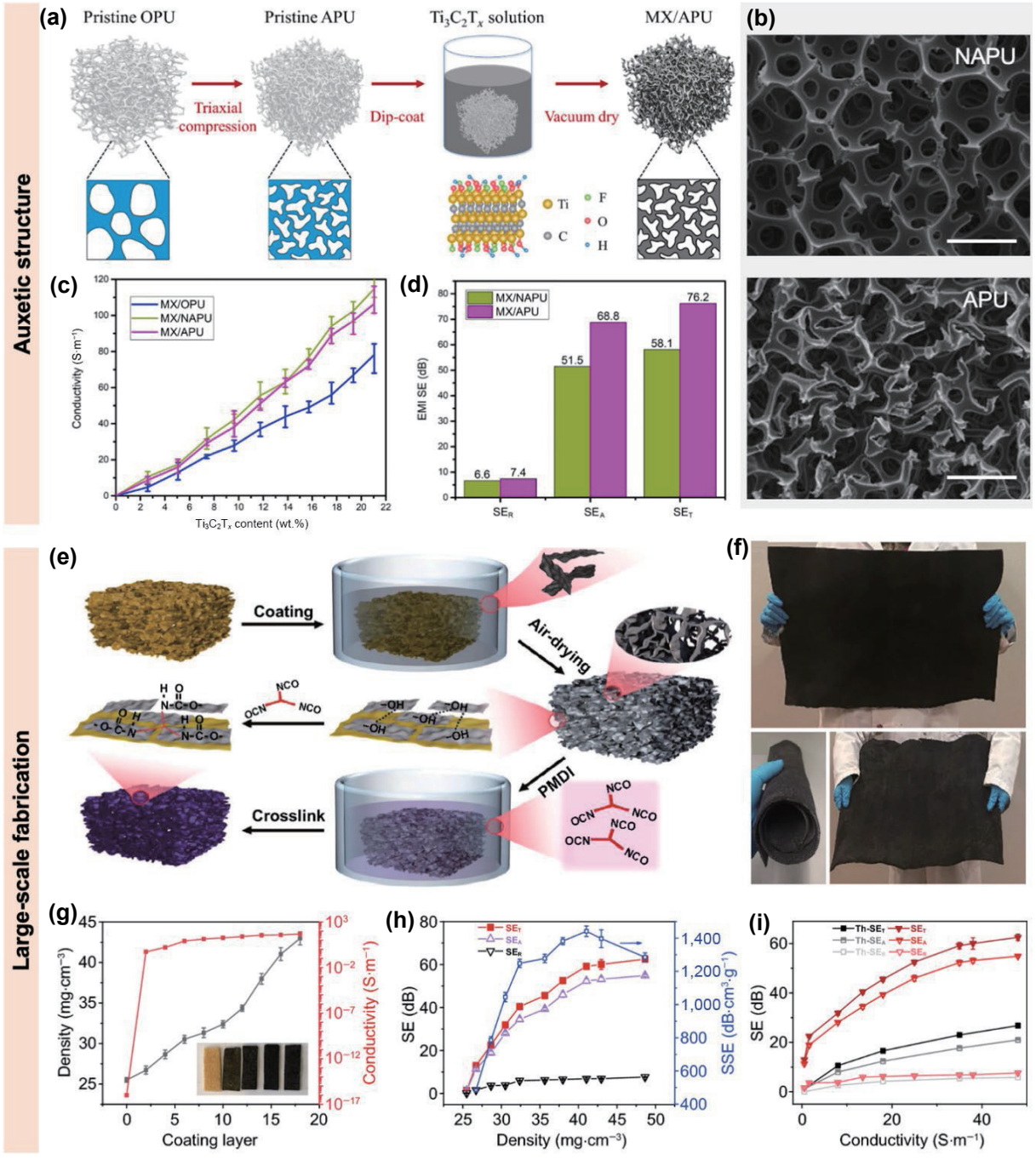

Figure 5 Fabrication of 3D foams by dip coating. (a) Schematics of the fabrication of MX/APU composite foam by triaxial compression and dip coating. (b) SEM images of NAPU and APU with a similar density. Scale bars: 500 μm. (c) Electrical conductivities and (d) EMI SEs of MX/NAPU and MX/APU foams. Reproduced with permission from Ref. [55], © Elsevier Ltd. 2021. (e) Schematics of the fabrication of a large-size $Ti_3C_2T_x$/PI composite foam by dip coating and chemical crosslinking. (f) Photographs of the large-size and flexible composite foam. (g) Densities and electrical conductivities of composite foams made by different dip-coating cycles. Each cycle corresponds to one layer of coating. (h) The EMI SEs and SSEs of composite foams with different densities. (i) Different components of EMI SEs obtained from theoretical calculations and experiments as a function of electrical conductivity. Reproduced from Ref. [80], © Zeng, Z. H. et al. 2022.

bidirectional, and radial freezing, which can ultimately afford tunable properties of the EMI shielding materials [36, 91, 98, 99]. A unidirectional freeze-casting (UFC) technique was used to fabricate a $Ti_3C_2T_x$/cellulose nanofibril (CNF) aerogel having orientation-dependent EMI shielding capabilities, as shown in Fig. 7(a) [36]. The unidirectional ice growth from the cold finger expelled solid $Ti_3C_2T_x$ and CNFs between the vertical ice columns, forming highly aligned hybrid walls with honeycomb cross-sections after freeze-drying (Figs. 7(a)(i)–7(a)(iii)). The highly anisotropic structure gave rise to more effective EMI shielding when EM waves propagated in the direction transverse to the alignment rather than parallel to it because of effective interactions of EM waves with the former (Fig. 7(b)). Therefore, the EMI SE values discussed in the following were measured when the incident EM waves were transmitted in the transverse to pore alignment direction unless otherwise specified. Moreover, the EMI SE also depended strongly on the orientation of the cell walls (Fig. 7(c)). When the angle between the cell walls and that of the electric field was 0°, i.e., the cell walls were aligned parallel to the electric field, a high EMI SE of 63 dB was achieved, as shown in Fig. 7(d). Interestingly, the EMI SE decreased consistently with increasing inclined angle, reaching the lowest value of 36 dB at 90°. This finding stemmed from the reduced absorption with increasing angle, while the reflection component remained almost constant regardless of the cell wall orientation. The excellent tunability can be utilized to build adaptive shielding materials with

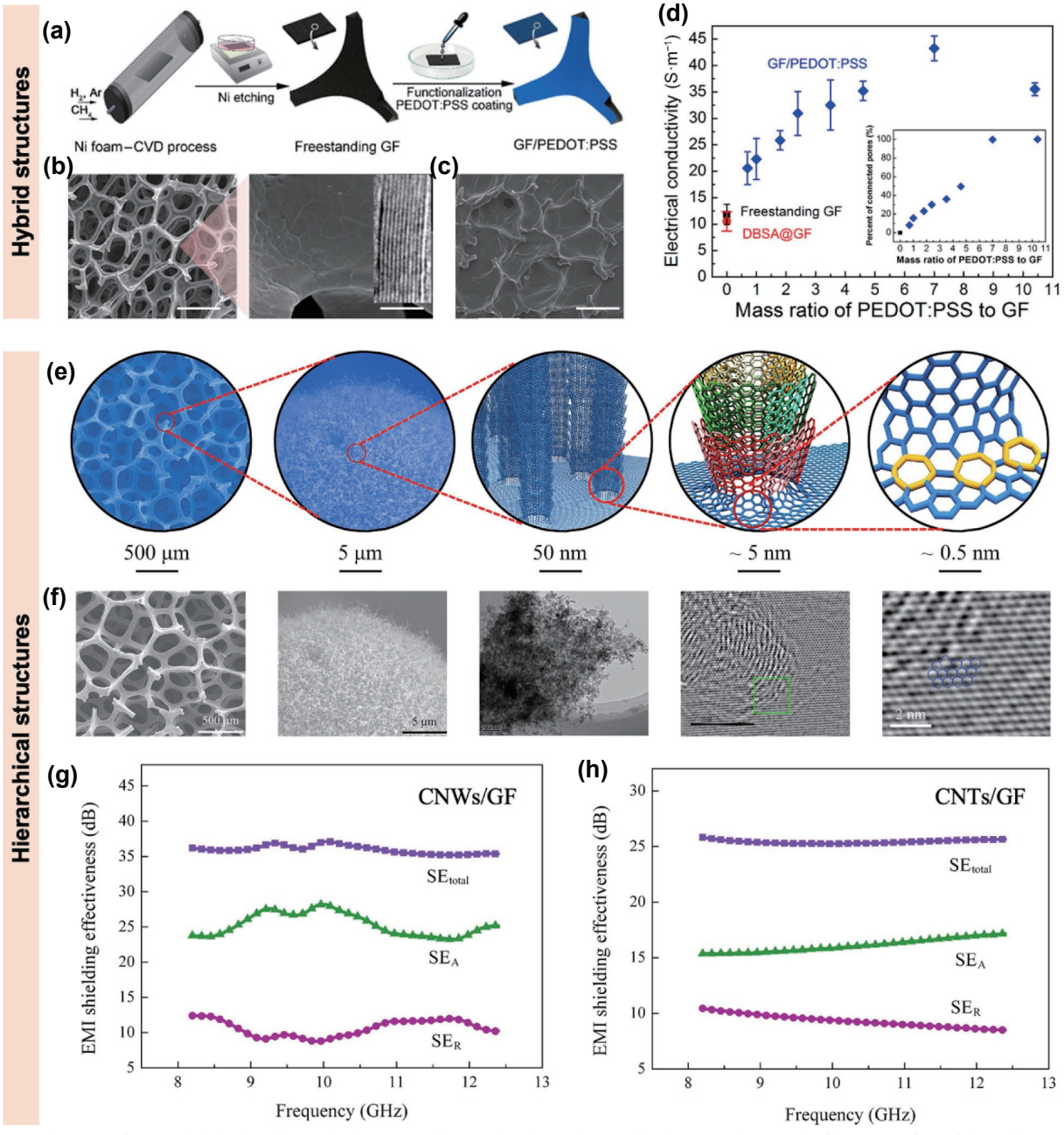

Figure 6 Fabrication of GFs with hybrid and hierarchical structures by template-directed CVD. (a) Schematics showing the fabrication of GFs followed by coating of PEDOT:PSS. SEM images of GFs (b) before and (c) after coating. Scale bars from left to right: 500, 30, and 500 μm. (d) Electrical conductivities of GF/PEDOT:PSS composites with different PEDOT:PPS to GF mass ratios. Reproduced with permission from Ref. [35], © American Chemical Society 2017. (e) Schematics and (f) SEM images showing the hierarchical structures of CNWs/GF at different length scales. The EMI SEs of (g) CNWs/GF and (h) CNTs/GF. Reproduced with permission from Ref. [88], © Elsevier Ltd. 2016.

well-regulated SEs by simply rotating the aerogel. With the capabilities to readily modulate the alignment, pore size, and cell wall thickness of 3D aerogels by tuning the freezing temperature and cooling rate, this technique has been widely used to fabricate graphene and MXene aerogels for EMI shielding applications [90, 98].

In addition to UFC, the bidirectional freeze-casting (BFC) approach was developed to construct porous structures from graphene and MXene nanosheets. Unlike the honeycomb cross-section derived from the unidirectional freezing, the BFC generated a highly lamellar structure owing to the dual temperature gradients in two orthogonal directions, as shown in Fig. 7(e) [99]. Different types of MXene, including $Ti_3C_2T_x$, Ti_2CT_x, and Ti_3CNT_x, were assembled into layer-structured aerogels with lamellar cell walls (Fig. 7(f)). The concentration of $Ti_3C_2T_x$ solution used for freeze-casting played a key role in determining the pore morphology. With increasing concentration, denser structures having shorter inter-lamellae spacings and more transverse interconnects were obtained (Fig. 7(g)). Among different MXene types, $Ti_3C_2T_x$ and Ti_2CT_x aerogels showed higher EMI SEs than that of Ti_3CNT_x (Fig. 7(h)), while an increase in density of $Ti_3C_2T_x$ aerogel gave rise to a higher EMI SE (Fig. 7(i)) because of the enhanced electrical conductivity. More importantly, the lamellar structure can be compressed and released reversibly along the transverse direction, providing controllable EMI absorption by altering the porosity through reversible compression. As shown in Fig. 7(j), the $Ti_3C_2T_x$ aerogels compressed to different thicknesses exhibited almost identical total SEs, but the contribution from absorption dropped with reducing thickness due to the diminishing porous structure. In summary, the highly aligned anisotropic structures obtained from uni- or bi-directional freeze-casting yielded not only high conductivities, but

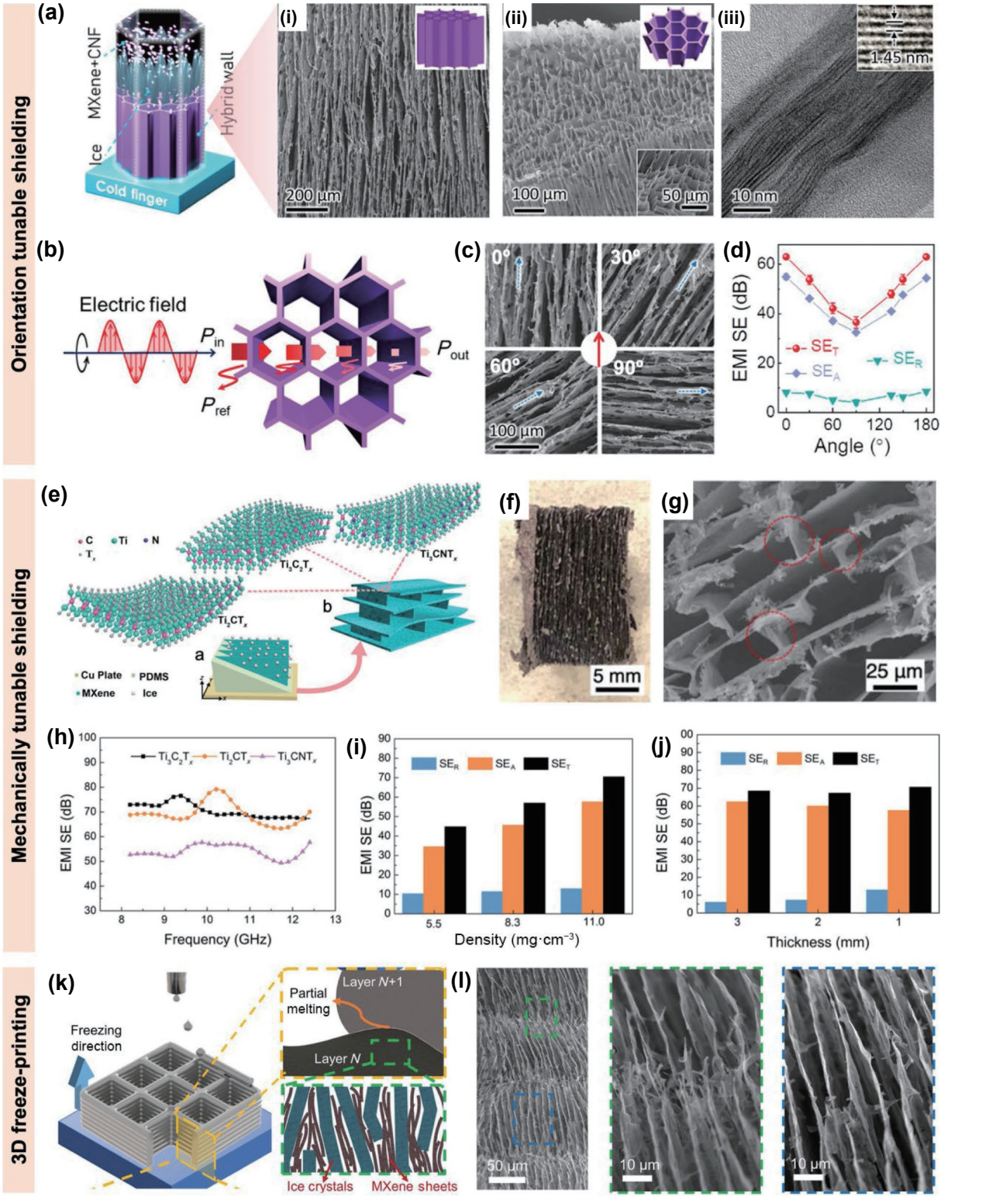

Figure 7 Assembly of 3D aerogels by freeze-casting for tunable EMI shielding. (a) Schematic of the UFC with (i) side- and (ii) top-view SEM images of the MXene/CNF aerogels and (iii) TEM image of the cell wall. (b) Schematics showing the directions of the EM wave propagation, electric field, and the cell wall alignment. (c) SEM images showing angles between the alignment of cell walls and the direction of electric field. (d) EMI SEs of the MXene/CNF aerogel as a function of angle shown in (c). Reproduced from Ref. [36], © Zeng, Z. H. et al. 2020. (e) Schematics of the fabrication of MXene aerogels by BFC. (f) Optical and (g) SEM images of the aerogel cross-section. EMI SEs of MXene aerogels with different (h) types, (i) densities, and (j) thicknesses. Reproduced with permission from Ref. [99], © WILEY-VCH Verlag GmbH & Co. KGaA, Weinheim 2019. (k) Schematics showing 3D freeze-printing of $Ti_3C_2T_x$ aerogel. (l) SEM images of the cross-section showing aligned $Ti_3C_2T_x$ cell walls with good interconnection between two layers because of the partial melting of the bottom layer upon the deposition of the top layer. Reproduced with permission from Ref. [100], © Wiley-VCH GmbH 2021.

also tunable shielding performance modulated by the orientation and mechanical compression in aerogels. The versatile freeze-casting technique can also be integrated with other methods, such as dip coating [79] and 3D printing [100], to construct more complicated yet desired structures. For example, a 3D freeze-printing technique combining 3D printing and unidirectional freeze-casting was developed to fabricate a $Ti_3C_2T_x$ aerogel, as shown in Fig. 7(k) [100]. The $Ti_3C_2T_x$ dispersion was injected from a printhead and deposited onto a cold metal plate on which the dispersion froze in the vertical direction to form aligned

$Ti_3C_2T_x$ cell walls. 3D macrostructure consisting of a series of vertically-aligned cell wall layers was produced through layer-by-layer deposition and freeze-casting (Fig. 7(l)). The partial melting of the frozen layer upon the deposition of a top layer ensured a good bonding between two successive layers and thus the mechanical robustness of the freeze-printed structure. The 3D freeze-printing technique was realized by proper controls of both macro- and microstructures of the aerogel, which would not be possible by either technique acting alone.

3.3 3D hydrogels

Hydrogels containing conductive fillers and confined water are emerging EMI shielding materials for wearable applications thanks to their excellent stretchability, conformability, biocompatibility, and self-healing capability [101, 102]. The large amount of water confined in the 3D conductive network of hydrogels can facilitate additional absorption of EM waves in GHz bands while serving as ion conduction channels to enhance the overall electrical conductivity [103, 104]. Two major approaches, including sol-gel assembly and additive manufacturing, have been developed to produce graphene and MXene-based hydrogels for multifunctional EMI shielding applications, and their details are discussed in the following.

Sol-gel assembly. The graphene- and MXene-based hydrogels can be readily made by a sol-gel process which involves self-assembly of large-size 2D nanosheets [102, 105]. During the sol-gel transition, crosslinked networks are formed through the interactions between 2D graphene or MXene sheets, which provide structural stability after gelation. For example, a graphene hydrogel was obtained from the self-assembly of rGO sheets with an area of ~ 200 μm² by virtue of strong π–π interactions between the large-size rGO [106]. For rGO or MXene sheets with smaller lateral dimensions, polymer molecules or ions were required to facilitate the gelation by linking the nanosheets with additional bonding mechanisms, which also offered extra stretchability and shape adaptability to the hydrogels. As shown in Fig. 8(a), a biomineralization-inspired process was developed by thoroughly mixing poly(acrylic acid) (PAA), chitosan (CS), and calcium chloride ($CaCl_2$) with a rGO solution before adding sodium carbonate (Na_2CO_3) for crosslinking and gelation of a rGO hydrogel [107]. The reaction product of $CaCl_2$ and Na_2CO_3, and amorphous calcium carbonate (ACC) formed strong crosslinking with PAA through chelation, while rGO sheets formed hydrogen bonds with PAA and CS, leading to excellent viscoelasticity of the hydrogel. Combined with a highly porous structure (Fig. 8(b)), the viscoelasticity enabled the hydrogel stretchable so that it could be processed to form different shapes and adapt to different surfaces (Fig. 8(c)). Furthermore, the reversible hydrogen bonds also effectuated fast self-healing when the two broken pieces were put together by gentle pressing (Fig. 8(d)) [108]. A similar sol-gel assembly process was used to fabricate a MXene-PAA-ACC hydrogel from $Ti_3C_2T_x$ nanosheets with shape formability and adhesiveness to different surfaces for wearable applications (Fig. 8(e)) [109]. Unlike the high electrical conductivity of $Ti_3C_2T_x$ films and aerogels, the MXene-PAA-ACC hydrogel showed moderate electrical conductivities of 0.001 to 0.008 $S{\cdot}cm^{-1}$ depending on the $Ti_3C_2T_x$ loading. Nonetheless, the porous structure and high water content contributed to a higher EMI SE than its foam counterpart of the same composition (Figs. 8(f) and 8(g)). The electrical conductivity of the hydrogel can be greatly improved by introducing ions in it to facilitate ionic conduction complementing the electronic conduction in the 3D network [110].

Despite the benefits of stretchability and self-healing, however, the easy evaporation and freezing nature of water makes hydrogels unappealing for applications in extreme temperature environments. To resolve the challenging issue, the water was replaced by organic solvents to improve the environmental tolerance of the hydrogel [37, 110]. For example, a MXene organohydrogel was prepared by replacing some of the water with glycerol (Gly), a common anti-freezing agent, via a solvent displacement method, as shown in Fig. 8(h) [37]. The volume of the hydrogel shrank after solvent displacement as the water content was reduced (Fig. 8(i)), while the porous structure remained intact in the organohydrogel (Fig. 8(j)). The freezing point of water was significant reduced owing to the hydrogen bonds between water and Gly, maintaining an excellent stretchability of the MXene organohydrogel even at a subzero temperature of −25 °C (Fig. 8(k)). Likewise, the MXene organohydrogel maintained a high EMI SE of 30.5 dB at −25 °C with no apparent decay from the value measured at room temperature (Fig. 8(l)). By contrast, a significant reduction of EMI SE from over 30 to 15 dB was observed in the MXene hydrogel, substantiating the advantage of the organohydrogel for tolerance towards the subzero-temperature environment.

Additive manufacturing. The foregoing self-assembly approach can produce hydrogels with high stretchability but is ineffective in controlling the micro- and macro-structures of the final product. Additive manufacturing is an emerging technique that can manipulate both the micro- and macro-structures for highly customizable EMI shielding. Among the most popular additive manufacturing techniques is the extrusion-based 3D printing, which has been widely used to fabricate graphene and MXene architectures [38, 100, 111, 112]. During the printing process, the viscous ink made from 2D nanosheet solution is ejected from a nozzle, continuously forming gel filaments on the substrate layer by layer with a predefined 3D pattern [113–116]. To ensure a mechanically stable hydrogel architecture, the rheological properties of the ink and proper post-printing treatment are critical. In terms of rheological properties, the ink needs to retain a shear thinning behavior with well dispersed 2D nanosheets. The concentration of 2D nanosheets in the aqueous ink can be adjusted to obtain proper rheological properties [117]. The 2D nanosheets can also be added into the polymer solution for improved printability. For example, the $Ti_3C_2T_x$ MXene solution was mixed with PEDOT:PSS to modify the viscosity of the ink, as shown in Fig. 9(a) [38]. The hydrogen bonds and electrostatic interactions between the functional groups on $Ti_3C_2T_x$ and PEDOT:PSS chains improved the shear thinning behavior of the ink at a low $Ti_3C_2T_x$ nanosheet concentration of only 1 wt.%, leading to a high modulus at a low shear rate and thus allowing the printed structure to keep its intended shape (Fig. 9(b)). Nevertheless, the secondary bonding nature between $Ti_3C_2T_x$ and PEDOT:PSS means a relatively weak as-printed pattern structure, which could be dismantled under vigorous stirring in water. To further improve the mechanical robustness, the post-treatment becomes an important step in addition to tuning the rheological properties of the ink. The acid treatment was effective in improving the crystallinity of PEDOT:PSS for better mechanical properties, but a large volume shrinkage was accompanied when applied directly to the hydrogel (Fig. 9(b)). A freeze-thawing process was therefore developed to allow mild gelation and acid treatment, as shown in Fig. 9(c). The freezing of as-printed hydrogel made the $Ti_3C_2T_x$ and PEDOT:PSS chains more compact pushed by the ice crystals, while the subsequent thawing in the H_2SO_4 solution slowly replaced the melted ice with acid, so that the shrinkage was prevented and the compact structure of the $Ti_3C_2T_x$ and PEDOT:PSS networks was maintained. Consequently, both the macro shape (Fig. 9(b)) and the microstructure of the filament (Fig. 9(d)) were well retained after

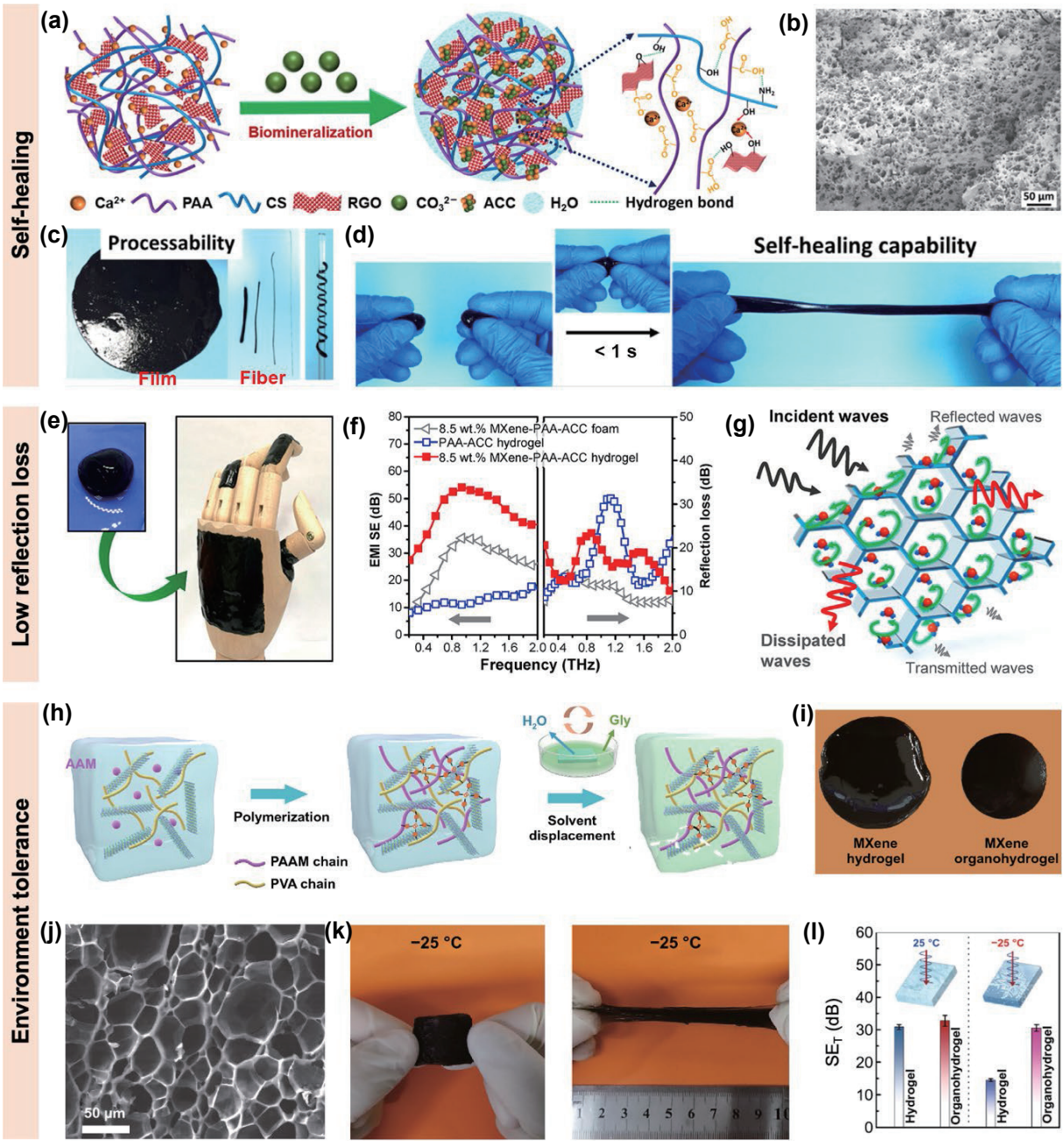

Figure 8 Fabrication of 3D hydrogels by sol-gel assembly. (a) Schematics of the fabrication of a rGO hydrogel by biomineralization-inspired sol-gel assembly. (b) SEM image of the rGO hydrogel. Photographs of the (c) processibility and (d) self-healing capability of the rGO hydrogel. Reproduced with permission from Ref. [107], © Elsevier Ltd. 2021. (e) Photographs showing a MXene hydrogel made by the biomineralization-inspired self-assembly and its excellent shape formability. (f) EMI SE and reflection loss of the MXene-PAA-ACC hydrogel in comparison with its foam and pristine PAA-ACC hydrogel counterparts. (g) Schematic of the shielding mechanism of the hydrogel. Reproduced with permission from Ref. [109], © American Chemical Society 2021. (h) Schematics of the fabrication of MXene organohydrogels by solvent displacement. (i) Optical and (j) SEM images of the MXene organohydrogel. (k) Optical images showing the MXene organohydrogel before and after stretching at −25 °C. (l) EMI SEs of MXene hydrogel and organohydrogel at ±25 °C. Reproduced from Ref. [37], © Yu, Y. H. et al. 2022.

freeze-thawing in acid. Another benefit of the acid treatment was the removal of non-conductive PSS chains, which in turn improved the electrical conductivity of the hydrogel from 0.26 to over 15 S·cm^{-1}. The boosted electrical conductivity directly enhanced the EMI SE to over 50 dB after high-concentration acid treatments (Fig. 9(e)). Compared to the freeze-dried foam samples after removing water, the hydrogel samples showed higher EMI SEs because of the positive effect of water in absorbing the EM waves (Fig. 9(f)). To summarize, the unique features of 3D-printed structures, including highly customizable macro-architectures and tunable microstructures, allowed precision shielding of complex device structures by conforming to their shapes (Fig. 9(g)). In addition, the 2D nanosheets could be aligned in the final hydrogel product because of the high shear forces acting during the printing process [118, 119], which in turn improves the electrical conductivities for better EMI shielding performance.

The advantages and disadvantages of different methods are tabulated in Table 1 to provide a general guideline in choosing proper methods to fabricate porous structures suitable for specific end applications. For 2D porous films, sacrificial templating is preferred when controllable pore sizes are required to achieve high SSE/t values, whereas self-assembly is more suitable for low-cost and large-scale shielding applications. Amongst different methods to fabricate 3D foams and aerogels, dip-coating is the most promising for scalable production. By contrast, template-directed CVD is costly to operate but can be useful when ultrahigh EMI SEs are needed. Freeze-casting is particularly advantageous when tunable EMI shielding is necessary as it can produce highly

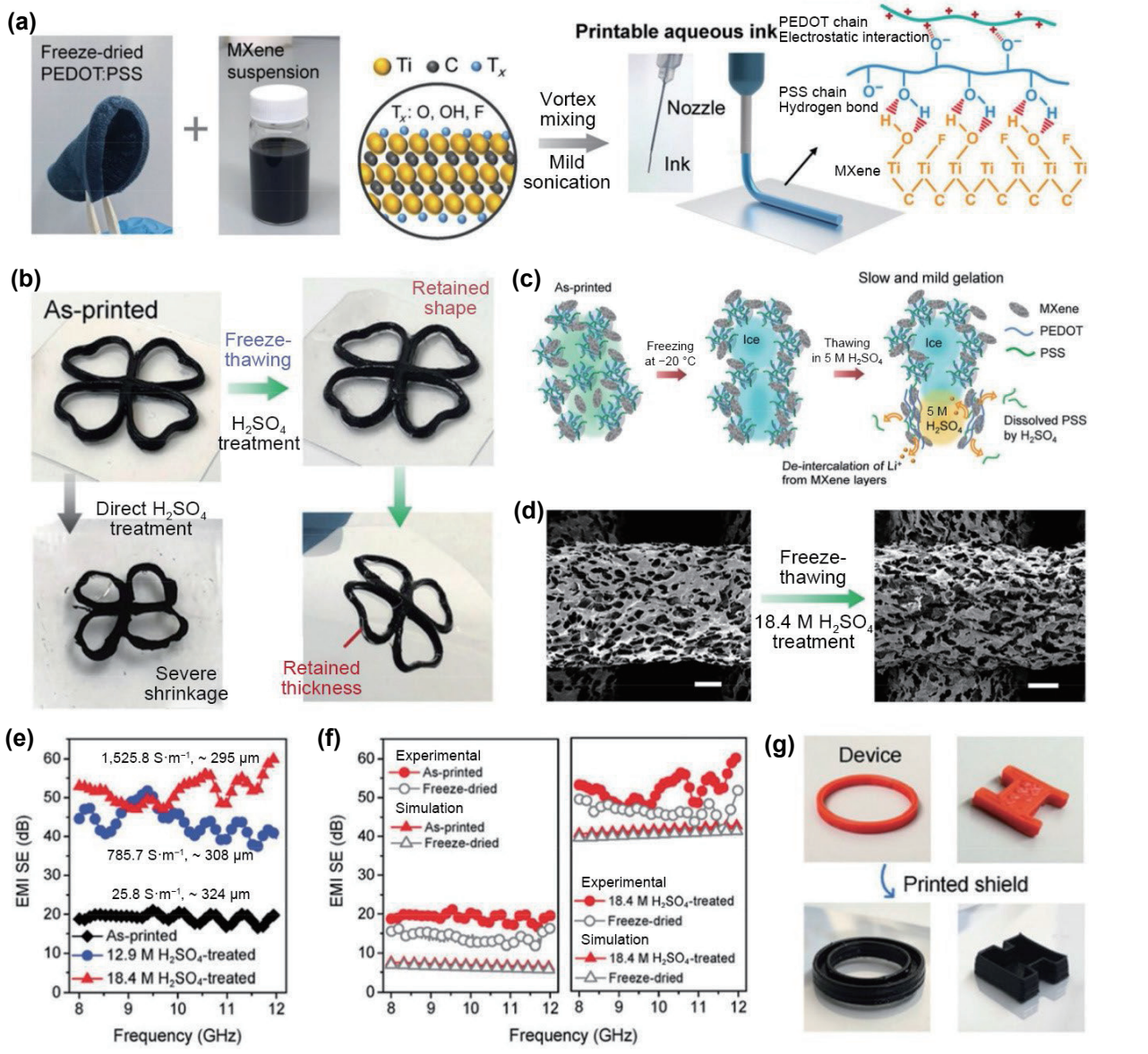

Figure 9 Fabrication of 3D hydrogels by additive manufacturing. (a) Schematics of the extrusion-based 3D printing of $Ti_3C_2T_x$/PEDOT:PSS hydrogel. (b) Optical images of hydrogels with direct H_2SO_4 treatment and freeze-thawing in H_2SO_4 solution. (c) Schematics of the freeze-thawing mechanisms. (d) SEM images of the filaments before and after freeze-thawing. Scale bars: 200 μm. EMI SEs of H_2SO_4-treated hydrogels in comparison with (e) as-printed hydrogel and (f) freeze-dried foams. (g) Optical images of 3D printed hydrogels for devices with different shapes. Reproduced with permission from Ref. [38], © Wiley-VCH GmbH 2021.

anisotropic structures. Hydrogels are more suitable than porous films or foams for stretchable shielding applications in emerging wearable electronics. The sol-gel assembly can produce highly stretchable shielding materials with a self-healing capability, while additive manufacturing is an effective choice when precision shielding of complex structures is needed owing to highly customizable macro-architectures.

4 Comparison of EMI shielding performance

To understand the effects of different processing methods and microstructures on the EMI shielding performance of porous structures made from graphene and MXene sheets, a comprehensive comparison is carried out in terms of their electrical conductivities, EMI SEs, and SSE/*t*, as shown in Table 2. Conventional metal-based EMI shielding films, such as steel and copper, showed exceptional EMI SEs of ~ 90 dB at thicknesses ranging 3–4 mm because of their high electrical conductivities in the orders of 10^6 to 10^7 S·m^{-1} [41]. However, the high densities of metals led to rather poor SSE/*t* values of only ~ 30 dB·cm^2·g^{-1}. Although the metal foam with a lower density than the solid film could achieve a SSE/*t* of over 700 dB·cm^2·g^{-1}, its absolute EMI SE remained only 25 dB, making it ineffective when a high SE is required [51]. Alternatively, lightweight carbon fiber-reinforced polymer composites achieved a balance between SE and density, delivering a high SE of 73.9 dB and a moderate SSE/*t* of 176 dB·cm^2·g^{-1}. With the emergence of highly electrically conductive fillers, including graphene and MXene, carbon fibers have been replaced by these nanofillers for much improved electrical conductivities of composites [4, 14–16]. In particular, a 2D compact $Ti_3C_2T_x$ film made by vacuum assisted filtration (VAF) exhibited an excellent EMI SE of over 50 dB at a thickness of 6 μm, giving rise to an SSE/*t* of over 30,000 dB·cm^2·g^{-1} thanks to the extra high electrical conductivity of the $Ti_3C_2T_x$ film in the order of 10^5 S·m^{-1} [16].

Compared to compact films, porous films made from graphene and MXene sheets generally showed higher SSE/*t* values owing to much lower densities arising from the high porosities. For porous MXene films, the foaming process [16] and polymer templating approach [62] yielded ultrahigh SSE/*t* values of over 100,000 dB·cm^2·g^{-1}, which were higher than those obtained from

Table 1 Comparison of different fabrication methods

Methods	Advantages	Disadvantages	Typical applications
2D porous films			
Sacrificial templating	• Cheap and widely available polymer sphere templates • Controllable pore size • Possible nanoscale pores in graphene film by CVD	• Template removal required by high-temperature annealing • Nanoscale pores depending on the availability of de-alloyed templates	Porous shielding films with controllable pore sizes for applications requiring high SSE/*t* values
Self-assembly	• Simple process • Good mechanical properties because of crosslinking by ions	• Post foaming process necessary for small-size MXene sheets • Difficult to control pore size	Porous shielding films for low-cost and scalable shielding applications
3D foams and aerogels			
Dip coating	• Simple process • Easy to control the pore morphology by manipulating the template structure • Scalable	• Relatively large pores • Non-freestanding final products	Customizable microstructures and scalable fabrication for applications requiring low-cost and large-scale shielding
Template-directed CVD	• High-quality graphene scaffolds • Secondary structures possible to further improve electrical conductivity	• High cost • Difficult to scale up • Not applicable to MXene structures	Superior conductivity for applications requiring ultrahigh EMI SEs
Freeze-casting	• Highly anisotropic pores • Simple and environmentally friendly process • Pore structures easily controlled by ice crystal growth dynamics	• Waterborne polymers required • Non-trivial to achieve long-range alignments • Freeze-drying needed to obtain porous structures	Aligned pore structures for orientation and mechanically tunable shielding
3D hydrogels			
Sol-gel assembly	• High stretchability and shape adaptability • Self-healing • Water replaceable by organic solvents for improved environment tolerance	• Extra ions/polymers needed to induce gelation for small-size graphene and MXene sheets • Relatively low electrical conductivity • Difficult to control pore structures	Highly stretchable EMI shielding with self-healing capability
Additive manufacturing	• Controllable micro- and macro-structures • Possible alignment of 2D sheets by shear forces during printing	• Fine tuning of ink rheology required • Post-treatment required for MXene structures	Customizable macro-architectures for precision shielding of complex device structures

self-assembly [73] or 3D printing [112]. For porous graphene films, the overall SSE/*t* values were not as high as the MXene counterparts because of the inherently lower electrical conductivity of graphene than MXene. Nevertheless, a high absolute SE of 83 dB was obtained by the CVD-grown porous graphene film, which was even higher than those of the porous MXene film [54]. The nano-sized pores in the graphene film contributed significantly to the absorption of EM waves through multiple scattering, confirming the positive effect of large surface areas in improving the EMI SE.

The SSE/*t* values of 3D porous aerogels and foams were overall lower than the porous films because of the millimeter thickness of porous aerogels and foams, much thicker than the micrometer-thick films. However, the large thickness of aerogels or foams in turn led to higher absolute EMI SEs than those of porous films. Among different methods, the template-directed CVD and directional freeze-casting were the two most effective techniques in fabricating GFs [35, 39, 40, 87] and MXene aerogels [36, 98, 99], respectively, both with high EMI SEs of over 70 dB. This observation can be attributed to the high-quality graphene produced by CVD and aligned networks of MXene sheets by freeze-casting. In particular, coating the high-quality GFs with conductive PEDOT:PSS yielded an unprecedented EMI SE of 91 dB [35], which is comparable to those of steel and copper films but with a much lower density.

Unlike porous films or foams, hydrogels made by sol-gel assembly or 3D printing from graphene and MXene solutions contained a large amount of water instead of air, making the densities of hydrogels much higher than porous films or aerogels. Although water contributed to EM absorption, it also lowered the electrical conductivity unless ions [110] or conductive polymers [38] were added in the hydrogel. Therefore, the EMI SEs of hydrogels were not as high as porous films, aerogels, or foams studied above. Nevertheless, the hydrogels had high stretchability, conformability, and self-healing capability [107, 109, 110], which were not attainable in porous films or aerogels. Hydrogels could also be made to form different shapes for highly customizable EMI shielding in electronics and wearable devices [37].

5 Multifunctional EMI shielding applications

The exceptional performance discussed above makes porous graphene and MXene composites and structures promising for EMI shielding applications. With the multifunctional properties of graphene and MXene as well as the unique microstructures achieved by rational assembly, the porous composites and structures made therefrom exhibited multifunctionalities beyond EMI shielding, enabling novel applications towards the advancement of wearable and smart electronic devices. The multifunctionalities include adaptive shielding, mechanical attenuation, thermal management, and wearable sensors, and the current section is dedicated to discussing these unique features of high-performance EMI shielding materials.

5.1 Adaptive shielding

The increasing complexity and precision of electronic devices mean new challenges for the next generation EMI shielding materials. Adaptive shielding materials with dynamic SEs enabled by external stimuli according to specific application requirements are superior to conventional shielding materials with static EMI SEs for smart EMI shielding applications, such as high-precision EM protection and active camouflage systems [31]. In particular, a large tuning range of EMI SE by external stimuli is useful for on-demand and switchable EMI shielding. EMI shielding materials

Table 2 Comparison of EMI shielding performance of graphene and MXene-based structures

Materials	Thickness, t (mm)	Density (g·cm^{-3})	Conductivity (S·m^{-1})	SE (dB)	SSE/t (dB·cm^2·g^{-1})	Fabrication method
Conventional shielding materials						
Steel [41]	4	7.9	1.8×10^6	88.9	28	—
Copper [41]	3.1	8.96	5.8×10^7	90.2	32	—
Ni-Cu foam [51]	1.5	0.23	—	25	724	—
Carbon fiber/PES [41]	2.85	1.47	—	73.9	176	—
2D compact films						
Monolayer graphene [18]	3.4×10^{-7}	2.26	5.25×10^6	2.3	3×10^7	TD CVD[a]
Graphene film [14]	0.05	2.2	1.14×10^5	62	5,636	TD CVD[a]
rGO film [15]	0.0084	2.1	1×10^5	20	11,337	Solution casting
rGO/epoxy [2]	> 0.1	1.5	1	38	2,533	Solution casting
$Ti_3C_2T_x$ film [4]	0.045	2.39	4.6×10^5	92	8,554	VAF
$Ti_3C_2T_x$ film [16]	0.006	2.39	4×10^5	53	36,960	VAF
$Ti_3C_2T_x$/SA [4]	0.008	2.31	2.9×10^5	57	30,844	VAF
rGO/PU [17]	1	1.6	16.8	34	212	Layer-by-layer assembly
2D porous films						
$Ti_3C_2T_x$ film [16]	0.06	0.22	58,000	70	53,030	Foaming
$Ti_3C_2T_x$ film [16]	0.006	0.39	58,800	32	136,700	Foaming
GF [78]	0.3	0.06	3,100	25.2	14,000	Foaming
rGO film [74]	0.2	0.048	1,050	47.8	49,750	Foaming
$Ti_3C_2T_x$-rGO film [34]	0.05	0.263	7,440	42.5	33,726	Foaming
rGO bubbles [60]	0.1	0.32	5,000	54	16,875	Polymer templating
MXene film [62]	0.05	0.1	47,000	60	120,000	Polymer templating
Porous graphene film [54]	0.3	0.045	3,300	83	61,630	TD CVD[a]
Porous graphene film [54]	0.035	0.049	3,600	17.3	100,875	TD CVD[a]
Graphene/PDMS film [53]	0.16	0.025	624.4	18	45,188	TD CVD[a]
$Ti_3C_2T_x$/rGO film [73]	0.06	0.26	40,000	59	37,619	Self-assembly
$Ti_3C_2T_x$ grid [112]	0.014	0.63	160,000	38.3	42,932	3D printing
3D porous foams and aerogels						
rGO/PEI [120]	2.3	0.29	1.75×10^{-6}	12.8	192	Interfacial assembly
MXene/PU [55]	10	0.063	106	76.2	1,210	Dip coating
Graphene/PU [56]	2	0.58	104.6	59.8	515	Dip coating
$Ti_3C_2T_x$/PI [80]	3	0.041	100	80.8	6,569	Dip coating
rGO/PU [81]	60	0.03	0.03	57.7	320	Dip coating
GNP/MF [82]	2	0.21	45.2	35.6	848	Dip coating
GF/PDMS [1]	3	0.06	200	33	1,833	TD CVD[a]
GF-CNT/PDMS [39]	1.5	0.09	3,150	75	5,555	TD CVD[a]
GF/PEDOT:PSS [35]	1.5	0.076	3,500	91	7,982	TD CVD[a]
GF-Fe_3O_4/PDMS [40]	2	1.18	8,400	70.4	298	TD CVD[a]
Fe_3O_4@$Ti_3C_2T_x$-GF/PDMS [87]	1	0.972	638	83.6	860	TD CVD[a]
CNW-GF/PDMS [88]	1.6	0.971	340	36	232	TD CVD[a]
CNT-SiC/GF [89]	2.5	0.95	224	32.1	135	TD CVD[a]
$Ti_3C_2T_x$/CNF aerogel [36]	2	0.008	108.7	74.6	46,600	UFC
	2	0.0015	1.17	35.5	118,167	
$Ti_3C_2T_x$ aerogel [98]	2	0.006	2,200	75	62,500	UFC
$Ti_3C_2T_x$-rGO [91]	2	0.03	695.9	56.4	9,400	UFC
$Ti_3C_2T_x$ aerogel [99]	1	0.011	—	70.6	64,182	BFC
Ti_2CT_x aerogel [99]	1	0.11	—	69.2	62,909	BFC
Ti_3CNT_x aerogel [99]	1	0.011	—	54.1	49,182	BFC
$Ti_3C_2T_x$ -rGO scaffold [111]	1.2	0.016	73	37.0	19,270	3D printing
	1.4	0.038	1,013	62.5	11,748	
3D hydrogels						
rGO hydrogel [107]	9.71	—	0.33	125	—	Sol-gel assembly
$Ti_3C_2T_x$ hydrogel [109]	0.13	—	0.8	45.3	—	Sol-gel assembly
GO/LiCl/PVA [110]	3	—	10.98	39.6	—	Sol-gel assembly
$Ti_3C_2T_x$ organohydrogel [37]	1	—	0.442	33.6	—	Sol-gel assembly
$Ti_3C_2T_x$/PEDOT:PSS hydrogel [38]	0.295	—	1,525.8	51.7	—	3D printing

[a]TD CVD = template-directed CVD

with tunable SEs by strain [81, 121, 122], temperature [21, 123, 124], and voltage [125] via altering the electrical conductivity have been reported. However, the range of tunable EMI SEs was narrow, making it difficult to employ as EMI shielding switches. The porous structure provided opportunities for designing new mechanisms to realize switchable EMI shielding. Several mechanisms and external stimuli, including orientation [36], moisture [126], and strain [127], have been proposed to control the EMI SE of porous shielding materials through manipulating the pore structures. The highly aligned pores of a MXene/CNF aerogel made by directional freeze-casting were exploited to tune the EMI SE by orienting the pore channels to different angles with the electric field when the EM wave propagated transverse to the aligned pores, as shown in Figs. 10(a) and 10(b). As the angle between the pore alignment and the electrical field was increased from 0° to 90° (Fig. 10(c)), the EMI SE significantly deteriorated from ~ 63 to 36 dB (Fig. 10(d)). The overall reduction in SE mainly arose from the drop in absorption component whereas the reflection shifted only slightly with the angle (Fig. 10(e), left panel). The inherently high absorption of EM waves was attributed to the strong and internally generated electric field when the cell walls aligned in parallel to the electric field dissipated the incident EM waves in the form of heat. On the contrary, the EMI SEs of the aerogel remained rather low at ~ 33 dB regardless of the angle when the EM wave propagated parallel to the aligned pores (Fig. 10(e), right panel). The orientation-controlled EMI SEs of the aligned MXene/CNF aerogel offered a facile route to tune the shielding performance on demand by simply rotating the shielding material without changing its shape or composition.

Despite the effortless control of EMI shielding by orientation, the lower bound of the EMI SE (~ 36 dB) was still too high to allow EM waves to penetrate. This means that the above strategy cannot be used when an EMI switch capable of toggling between transmission and shielding is required. To achieve switchable EMI shielding, a hydro-sensitive sandwich structure was developed consisting of conductive pyrolytic graphite (PG) paper faces and a rGO/CNT/non-woven (NW) polypropylene porous core, as shown in Fig. 10(f) [126]. The G-rGO/NT/NW-G sandwich structure exhibited a SE of ~ 20 dB in the dry state (State-1, Fig. 10(f)), indicating weak EMI shielding performance. After introducing water of different loadings into the porous structure (State-2 and -3), the EMI SEs increased to over 30 dB thanks to the water-induced polarization. The switch between weak and strong shielding was reversible when the porous structure was dried completely with a recovered EMI SE of ~ 20 dB, demonstrating the effectiveness of the hydro-sensitive structure for smart EMI shielding. Its switching range was extended using mechanical force as the stimuli. A carbon aerogel was made by depositing carbon black particles on a hydrothermally-treated wood followed by annealing, producing a lamellar structure with wavy amorphous carbon fibrils decorated with conductive particles (Fig. 10(g)) [127]. The carbon aerogel was highly compressible along the transverse direction because of the lamellar structure, resulting in a concomitant rise in electrical conductivity with increasing compressive strain because of the percolation of conductive carbon black when highly compressed, as shown in Fig. 10(g). The improved electrical conductivity translated into an improved EMI SE from 1.4 to 27.6 dB when the compressive strain was 75% (Fig. 10(h)), indicating a transition from transmission to shielding of EM waves. Based on the above mechanism, an EMI shielding switch was made possible by compressing and releasing the carbon aerogel, showing excellent reversibility and repeatability (Fig. 10(i)). The on-demand response of EMI SE by the compressive force was critical to adaptive shielding to satisfy the real-time requirements of smart electronics.

5.2 Mechanical attenuation

One of the major advantages of porous structures over films for EMI shielding is their capabilities to protect the delicate electronic components from mechanical impacts by leveraging the high porosity, mitigating possible damages in service. There are two types of energy absorption mechanisms for porous structures to dissipate the mechanical energy. In the first mechanism, the impact energy is absorbed in the form of elastic energy by reversible deformation of struts or ligaments, thus highly compressible porous structures capable of returning to their original shapes are favored. As shown in Fig. 11(a), a MXene/rGO scaffold was developed from $Ti_3C_2T_x$ and GO sheets by 3D printing, showing interconnected filaments with porous cross-sections [111]. The interconnected filaments and integrated $Ti_3C_2T_x$/GO cell walls permitted a large reversible deformation under compression (Fig. 11(b)). The degree of reversible deformation was affected by the MXene content in the $Ti_3C_2T_x$/GO cell walls, as shown in Fig. 11(c). A low MXene content of 10% led to negligible plastic deformation under a compressive strain of 50%, suggesting a full recovery to the initial state after releasing the load. By contrast, higher MXene contents led to larger plastic deformation because of stiffer structures, resulting in irreversible deformation detrimental to elastic energy absorption. Impressively, the MXene/rGO scaffold with a low MXene content exhibited excellent elasticity under compression up to 90% strain (Fig. 11(d)), and consistent performance under cyclic compression to a maximum strain of 50% for 100 cycles (Fig. 11(e)). The excellent elasticity of the MXene/rGO scaffold was able to protect the electric circuits by absorbing the kinetic energy of an impinging steel ball and storing it elastically in the structure, as shown in Fig. 11(f). The ball was eventually bounced back once the elastic energy was released when the structure returned to its original shape without damaging the circuit board, as proven by the illuminated light-emitting diode (LED) light. In addition to 3D printing, other methods such as dip coating [81, 128, 129], template-directed CVD [130], directional freeze-casting [131], and sacrificial templating [132] were also effective in constructing highly elastic porous structures from graphene and MXene.

The second strategy to mitigate impact damages is to reduce the impact force exerted on the porous structure by micro-structural design [133–136]. An auxetic structure was incorporated into the MXene/PU foam (termed MX/APU) having inward protruding struts by triaxial compression and dip coating, as shown in Fig. 11(g) [55]. The struts in the auxetic foam rotated inward to induce lateral contraction so that lower forces were required to densify the porous structure than the non-auxetic foam which instead expanded laterally with bending or buckling deformation of struts (Fig. 11(h)). Such a unique deformation mechanism allowed the MX/APU foam to more effectively dissipate the impact energy, which is potentially useful for simultaneous EMI and impact attenuation applications (Fig. 11(i)). As shown in Fig. 11(j), the peak force in the MX/APU foam during an impact drop test was reduced by 51% compared to the NAPU under the same impact energy. For practical applications, this also means higher energy absorption in the MX/APU foam than NAPU (Fig. 11(k)), making it a more effective impact attenuator. Combined with the excellent electrical conductivity of MXene, the MX/APU foam demonstrated excellent EMI SE of 76 dB together with a high impact force attenuation capability.

5.3 Thermal management

With the emergence of 5G technology and widespread integration of electronic components, thermal management has become

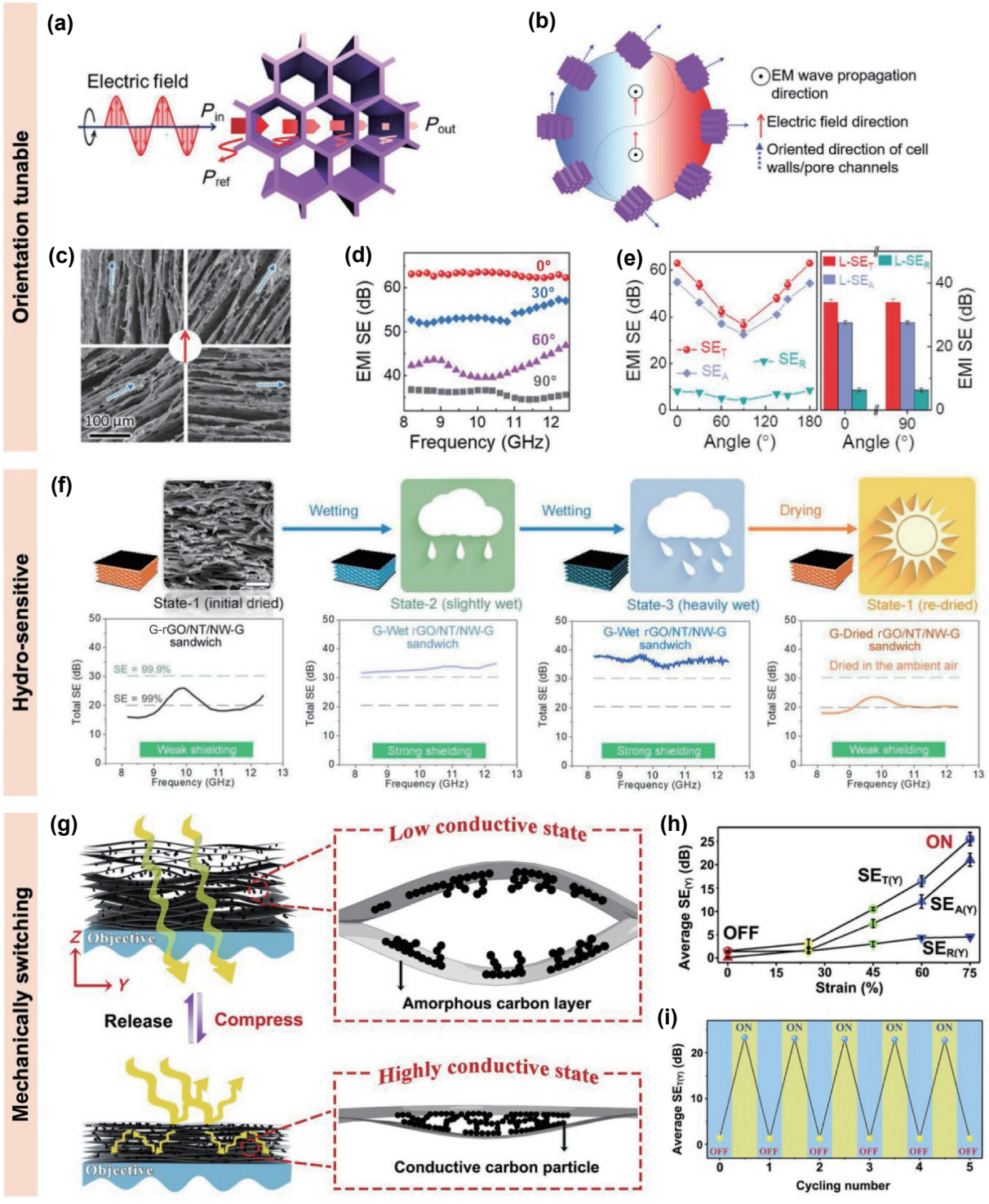

Figure 10 (a) Schematics showing the directions of the EM wave propagation, electric field, and the aligned pores. (b) Schematics and (c) SEM images showing the change in angles between aligned pores and electric field. (d) EMI SEs of aerogels oriented at different angles to the electric field. (e) Reflection, absorption, and total SEs of aerogels oriented at different angles to the electric field when the EM waves propagate transverse (left panel) and parallel (right panel) to the aligned pores. Reproduced from Ref. [36], © Zeng, Z. H. et al. 2020. (f) Schematics and EMI SEs of the hydro-sensitive sandwich structure under different conditions. Reproduced with permission from Ref. [126], © Elsevier B.V. 2018. (g) Schematics showing the switching mechanism of EMI SE in the carbon aerogel induced by compression. (h) EMI SEs as a function of compressive strain. (i) EMI SEs of the aerogel under compression/release cycles. Reproduced with permission from Ref. [127], © Elsevier Inc. 2021.

critical to either dissipate the heat generated from individual components or isolate the heat between components to avoid thermal interference [137]. Therefore, integrating thermal management capabilities into EMI shielding materials is promising to achieve multifunction in a limited space as the electronics continue to miniaturize [138]. Depending on the end applications, different thermal conductivities are required in the EMI shielding materials. For efficient heat removal, a high thermal conductivity is preferred, which necessitates the construction of fillers having high thermal conductivities into an interconnected network [139]. In addition, the porosity needs to be minimized to limit the contribution of low-thermal-conductivity air. In view of the above, graphene and its derivatives can be good fillers for achieving both EMI shielding and heat dissipation in porous structures because of their excellent electrical and thermal conductivities [140]. A microcellular graphite nanoplatelet

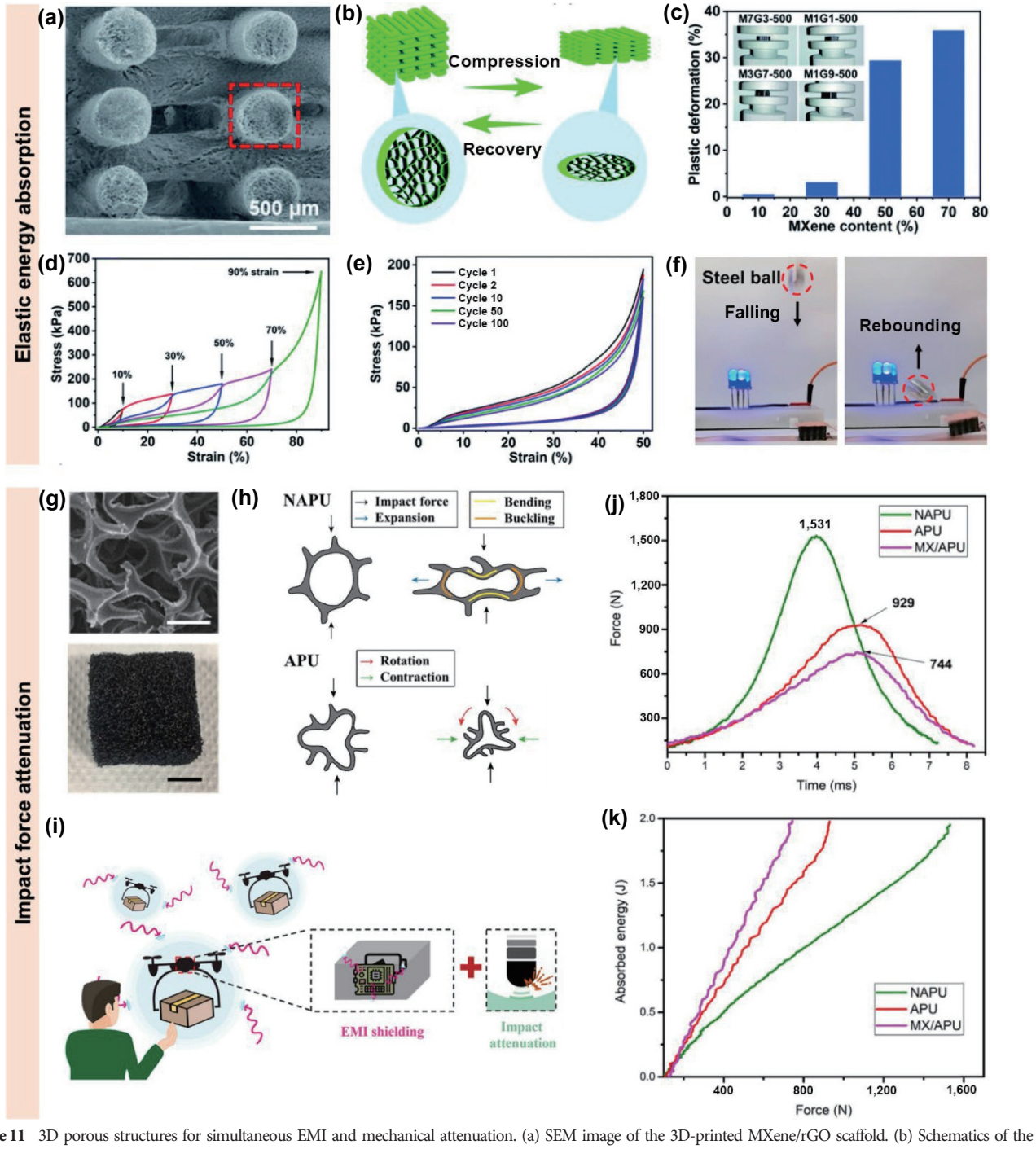

Figure 11 3D porous structures for simultaneous EMI and mechanical attenuation. (a) SEM image of the 3D-printed MXene/rGO scaffold. (b) Schematics of the elastic recovery of the scaffold under compression. (c) Plastic deformation in the MXene/rGO scaffolds with different MXene contents under a 50% compressive strain. Stress–strain curves of the MXene/rGO scaffold under (d) different compressive strains and (e) different cycles. (f) Photographs showing the excellent elastic energy absorption and recovery of the scaffold when impinged by a steel ball. Reproduced with permission from Ref. [111], © The Royal Society of Chemistry 2022. (g) SEM and optical images of the MX/APU foam. Scale bars: 200 μm (top) and 10 mm (bottom). (h) Schematics of the deformation mechanisms of NAPU and APU. (i) Schematics of dual attenuation of EM waves and impact energy for practical applications. (j) Peak forces and (k) absorbed energies of MX/APU, NAPU and APU. Reproduced with permission from Ref. [55], © Elsevier Ltd. 2021.

(GNP)/high-density polyethylene (HDPE) composite foam was developed by super critical fluid foaming in an injection molding process, resulting in distinctively gradient porous structures along the injection direction (Fig. 12(a)) [141]. At a distance, L, away from the gate, say L = 20 mm, the GNPs were oriented along the injection flow in the vicinity of the mold wall because of the shear force, while random orientation was dominant away from the wall, forming a core–shell structure. Looking further away from the gate, the aligned GNP shell decreased in thickness, eventually leading to random orientation of GNPs across the whole thickness when L = 100 mm. The unique variation of microstructures of the foam depending on the distance from the gate brought about different EMI SEs and thermal conductivities, as shown in Figs. 12(b) and 12(c). The random arrangement of GNPs was beneficial to the formation of interconnected networks, contributing to better percolation of the foam obtained at a long distance from the gate. This in turn translated into higher EMI SEs and thermal conductivities of the foam with random GNP orientation than those with core–shell structures. Overall, a high SSE/t of ~ 61 dB·cm^2·g^{-1} and thermal conductivity of 3.8 W·m^{-1}·K^{-1} were achieved in the GNP/HDPE foam with a GNP volume fraction of 19% and a low porosity of 7%. Other porous EMI shielding

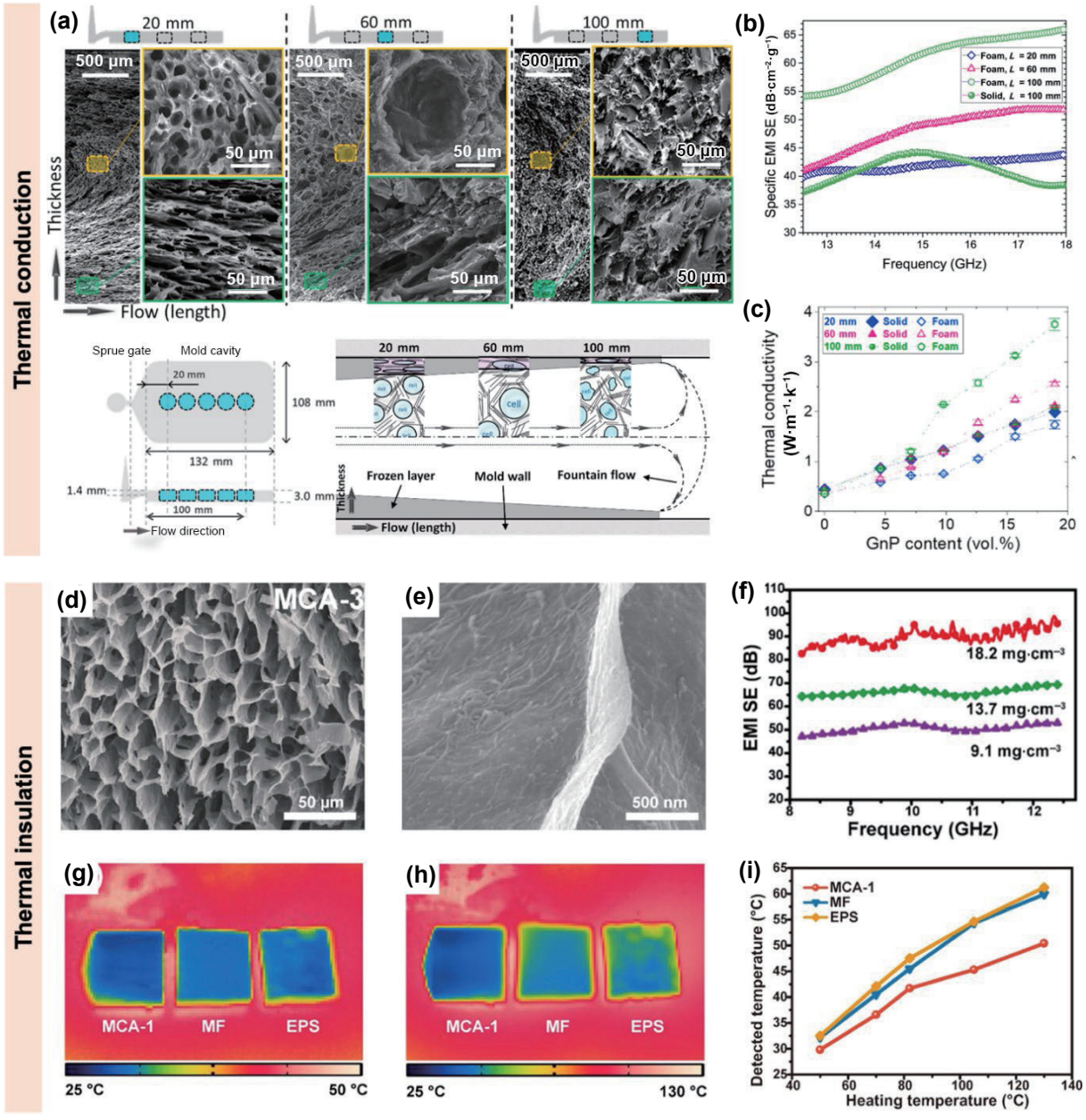

Figure 12 (a) SEM images of the GNP/HDPE composite foam with gradient microstructures along the length of flow and the schematics showing the mechanisms of super-critical fluid assisted injection molding. (b) Specific EMI SEs and (c) thermal conductivities of the foams produced at different lengths from the gate. Reproduced with permission from Ref. [141], © Elsevier Ltd. 2021. SEM images of the MCA showing (d) the porous cross-section and (e) MXene/CNT hybrid cell walls. (f) EMI SEs of the MCAs with different densities. Infrared images showing the surface temperatures of the MCA compared to commercial MF and EPS foams when placed on hot plates with temperatures of (g) 50 and (h) 130 °C. (i) Surface temperatures of MCA, MF, and EPS foam as a function of heating temperature. Reproduced with permission from Ref. [147], © American Chemical Society 2021.

materials made from dip coating [83], freeze-casting [142], self-assembly [143, 144], foaming [145, 146], and template-directed CVD [40] had relatively low thermal conductivities because of their high porosities. They were mostly used as 3D fillers to enhance the thermal conductivities of polymer composites by infiltrating polymers into the pores.

On the other hand, low thermal conductivities are sometimes required for EMI shielding materials to isolate the heat between electronic components. Highly aligned porous structures are particularly useful for thermal insulation because of the reduction of heat transfer in the transverse direction [93]. A MXene/CNT aerogel (MCA) was made by UFC, presenting highly aligned pore channels (Fig. 12(d)) and hybrid cell walls consisting of $Ti_3C_2T_x$ nanosheets and CNTs (Fig. 12(e)) [147]. The high electrical conductivities of both $Ti_3C_2T_x$ and CNTs translated into high EMI SEs of the MCAs, as shown in Fig. 12(f). It rose with increasing density, reaching an exceptional 90 dB on average over the whole X-band at a low density of 18.2 mg·cm^{-3}. Meanwhile, the porous MCA showed an excellent thermal insulation performance compared to commercial melamine foam (MF) and expanded polystyrene (EPS) foam, as indicated by the surface temperature difference when placed on a hot plate at 50 and 130 °C (Figs. 12(g) and 12(h)). At a plate temperature of 130 °C, the surface temperature of MCA was less than 50 °C, lower by over 10 °C than the MF and EPS counterparts, as shown in Fig. 12(i). The multifunctionalities enabled by the anisotropic MCA were particularly useful for electromagnetic and thermal protection in harsh environments [142, 148]. Other techniques, such as foaming [149, 150] and dip-coating [129, 151, 152], were also used to produce electrically conductive yet thermally insulating foams for EMI shielding applications.

5.4 Wearable sensors

Integrating sensory functions into EMI shielding structures is desired for multifunctional devices in wearable applications [153, 154]. The highly conductive porous structures used for EMI shielding are naturally suited for various sensory applications, such as strain, temperature, and humidity sensing [155]. To make the multifunctional sensors wearable, two types of sensors were developed based on (i) skin-mountable materials with high stretchability and shape adaptivity; and (ii) textile-based materials by integrating functional fillers with intrinsically wearable textiles. As shown in Fig. 13(a), a MXene hydrogel was fabricated by self-assembly of $Ti_3C_2T_x$ nanosheets and PVA for skin-mountable EMI shielding and strain sensing [109]. The MXene hydrogel was highly stretchable and malleable, which could be attached to complex surfaces such as finger joints while remained conformable under large deformation caused by the joint movements (Fig. 13(b)). On the contrary, the MXene film in Fig. 13(c) presents a completely different behavior with fracture under the same joint movement. The change of electrical resistance in the MXene hydrogel increased almost linearly with increasing uniaxial strain up to 300%, giving rise to a corresponding gauge factor of 5. The resistance changes were highly consistent for multiple cycles under different strains, demonstrating the repeatability of the MXene hydrogel (Fig. 13(d)). The hydrogel sensor was able to differentiate the motions of the finger joint when bent to different degrees, indicating its applicability for human motion monitoring (Fig. 13(e)). Other porous 2D films and 3D structures made by 3D printing [112, 156], dip-coating [75, 80, 157], freeze-casting [158, 159], and laser scribing [160] have also shown promising applications in skin-mountable EMI shielding and strain sensing devices thanks to their highly conductive networks.

In addition to skin-mountable sensors, textile-based sensors integrated with an EMI shielding capability were also developed by exploiting the inherent wearability of textiles. Conductive fillers

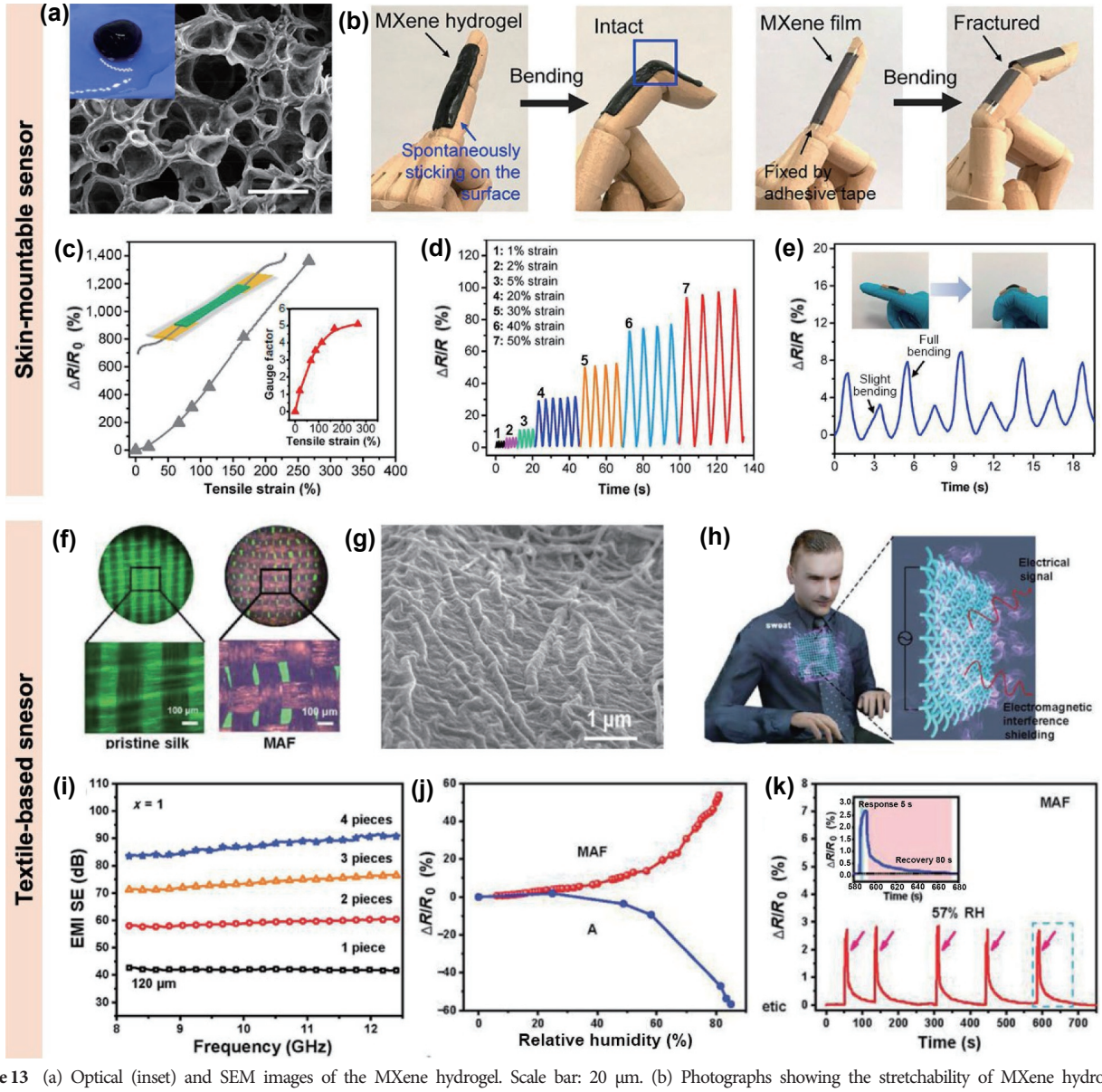

Figure 13 (a) Optical (inset) and SEM images of the MXene hydrogel. Scale bar: 20 μm. (b) Photographs showing the stretchability of MXene hydrogel in comparison with MXene film. (c) Resistance change of the hydrogel under uniaxial tension. The inset shows the gauge factor as a function of applied strain. (d) Resistance changes under cyclic tensions at different strains. (e) Resistance changes of the hydrogel attached to the finger joint in response to bending of fingers. Reproduced with permission from Ref. [109], © American Chemical Society 2021. (f) Optical microscopic images of pristine and MAF silks. (g) SEM image of the surface of MAF fibers. (h) Schematics of the breathability and EMI shielding capabilities of MAF silks for wearable applications. (i) EMI SEs of MAF silk textiles. (j) Resistance change of the MAF silk sensor in response to relative humidity. (k) Resistance change of the MAF sensor under cyclic humidity tests. Reproduced with permission from Ref. [163], © WILEY-VCH Verlag GmbH & Co. KGaA, Weinheim 2019.

were directly dip-coated or spray-coated onto their surface to offer the textile with electrical conduction [161, 162]. Nevertheless, the intrinsic breathability of the textile was impaired to a certain extent when the fillers blocked the space between yarns. To improve the electrical conductivity of textile without degrading the intrinsic breathability, a vacuum assisted layer-by-layer assembly technique was developed to incorporate 1D Ag nanowires (AgNWs) and 2D $Ti_3C_2T_x$ MXene sheets into silk textiles [163]. As shown in Fig. 13(f), large open pores between the fiber bundles remained intact in the MXene/AgNWs coated silk textile after hydrophobic treatment (termed MAF silk) compared to the original silk textile, although smaller slits between individual fibers disappeared after coating. The SEM images showed uniform deposition of 1D AgNWs and 2D $Ti_3C_2T_x$ sheets on the textile fiber surface, forming interconnected conductive networks for a much-improved electrical conductivity (Fig. 13(g)). The excellent permeability of air and high electrical conductivity enabled the MAF to effectively shield EM waves without causing discomfort (Fig. 13(h)). The EMI SE of a single layer of MAF silk with a thickness of only 120 μm reached 42 dB and increased monotonically to over 80 dB with increasing number of layers (Fig. 13(i)). Meanwhile, the MAF silk showed a characteristic surge in resistance with increasing relative humidity, making it suitable for humidity sensing in addition to EMI shielding (Fig. 13(j)). The water molecules could intercalate into the $Ti_3C_2T_x$ layers, causing the change in conductive network and augmenting the electrical resistance. The resistance change remained stable and consistent under cyclic tests with a response time of 5 s, suggesting a reliable humidity sensing capability of the MAF silk (Fig. 13(k)). In addition to humidity sensing, other EMI shielding textiles made from MXene and rGO also demonstrated impressive sensitivities towards external forces for strain and pressure sensing [164–167].

6 Conclusions and perspectives

In summary, we have reviewed the recent progress empowering the development of porous composites and structures from emerging 2D graphene and MXene sheets for multifunctional EMI shielding applications. Major EMI shielding mechanisms of porous structures, including conduction loss, interfacial polarization, and multiple reflection, are probed with thorough discussion on their correlations with critical material parameters, such as electrical conductivity, interfaces and functional groups, and pore structures. Different assembly techniques to obtain bulk porous structures, such as 2D porous films, 3D aerogels or foams, and hydrogels, are summarized to highlight the effects of different assembly techniques on critical material parameters and thus the EMI shielding performance through controlling the microstructures and pore morphologies. A comprehensive comparison of different assembly techniques is carried out to highlight their respective advantages and disadvantages, providing a practical guideline for the selection of methods most suitable for specific end applications. The EMI SE and SSE/t values of different porous structures are also benchmarked to quantitatively compare relative performance of different assembly techniques. CVD and freeze-casting are considered as the two most effective techniques to create 3D structures with high-quality graphene and aligned networks of MXene sheets, respectively, leading to higher EMI SEs than other techniques. Finally, the unique multifunctional properties of graphene and MXene allow the addition of other functionalities beyond simple EMI shielding in the porous structures, demonstrating novel applications in adaptive shielding, mechanical attenuation, thermal management, and wearable sensors. Notwithstanding the significant efforts and successful demonstration of graphene and MXene-based porous EMI shielding materials, several issues need to be resolved to deepen the understanding of shielding mechanisms for broader applications.

First, theoretical models accurately depicting the contribution from multiple reflection in the porous structures need to be developed. The current model widely used to calculate the EMI SE of porous structure is based on the Simon's formula [168], which only takes into account the electrical conductivity of materials and its effect on reflection and absorption. This consistently leads to underestimation of the actual EMI SEs because multiple reflection within the porous structures is considered as a predominant source of EM absorption [38]. However, there still lacks an accurate model to quantify the effects of various pore parameters, including pore size, porosity, and surface area, on the EMI shielding performance. The establishment of such correlations is critical to the rational design of porous EMI shielding materials with desired microstructures.

Second, one important benefit of using porous structures is the absorption-dominant EMI shielding capability while minimizing the reflection to reduce the secondary EM pollution [5]. However, it is still a formidable task to completely eliminate the reflection using porous structures. This is because a high electrical conductivity required for absorption inevitably causes reflection of EM waves by the conductive surfaces. Therefore, novel surface design approaches utilizing unique material characteristics and morphological features are required to minimize the reflected waves so as to fabricate near-zero-reflection EMI shielding materials [169, 170].

Third, despite the generally better performance of MXene than graphene in achieving high EMI SEs, the process and stability of many MXene sheets, including the most common $Ti_3C_2T_x$, are rather poor compared to rGO sheets. Simple fabrication processes yielding highly stable MXene sheets need to be developed to fulfill the requirement of large-scale production for practical applications. In addition, more varieties of MXene other than a handful types, such as $Ti_3C_2T_x$, Ti_2CT_x, and Ti_3CNT_x, need to be further explored for EMI shielding applications [99].

Last, most past and current efforts have been focused on EMI shielding in the X-band frequencies ranging 8–12 GHz. With widespread adoption of 5G technology and Terahertz devices, materials with frequency-selective shielding are highly desired [171, 172]. Moreover, the increasing demands for miniaturization of electronic components and devices and high flexibility of future electronics mandate smart shielding materials with tunable and anisotropic SEs as well as highly customizable shapes for on-demand shielding [36, 38, 127]. These unprecedented multiple requirements pose new challenges to devising porous EMI shielding materials, which necessitate novel structural designs and assembly techniques to achieve the desired properties.

Acknowledgements

This project was financially supported by the Research Grants Council (GRF Projects: 16205517, 16209917, and 16200720) and the Innovation and Technology Commission (ITS/012/19) of Hong Kong SAR, and start-up fund for new recruits of PolyU (Nos. P0038855 and P0038858). This project was also supported by the Research Institute for Sports Science and Technology of PolyU (No. P0043535).

References

[1] Chen, Z. P.; Xu, C.; Ma, C. Q.; Ren, W. C.; Cheng, H. M. Lightweight and flexible graphene foam composites for high-performance electromagnetic interference shielding. *Adv. Mater.* **2013**, *25*, 1296–1300.

[2] Yousefi, N.; Sun, X. Y.; Lin, X. Y.; Shen, X.; Jia, J. J.; Zhang, B.; Tang, B. Z.; Chan, M.; Kim, J. K. Highly aligned graphene/polymer nanocomposites with excellent dielectric properties for high-performance electromagnetic interference shielding. *Adv. Mater.* **2014**, *26*, 5480–5487.
[3] Chung, D. D. L. Electromagnetic interference shielding effectiveness of carbon materials. *Carbon* **2001**, *39*, 279–285.
[4] Shahzad, F.; Alhabeb, M.; Hatter, C. B.; Anasori, B.; Man Hong, S.; Koo, C. M.; Gogotsi, Y. Electromagnetic interference shielding with 2D transition metal carbides (MXenes). *Science* **2016**, *353*, 1137–1140.
[5] Chen, Y. M.; Yang, Y.; Xiong, Y.; Zhang, L.; Xu, W. H.; Duan, G. G.; Mei, C. T.; Jiang, S. H.; Rui, Z. H.; Zhang, K. Porous aerogel and sponge composites: Assisted by novel nanomaterials for electromagnetic interference shielding. *Nano Today* **2021**, *38*, 101204.
[6] Zheng, Q. B.; Li, Z. G.; Yang, J. H.; Kim, J. K. Graphene oxide-based transparent conductive films. *Prog. Mater. Sci.* **2014**, *64*, 200–247.
[7] Zheng, Q. B.; Lee, J. H.; Shen, X.; Chen, X. D.; Kim, J. K. Graphene-based wearable piezoresistive physical sensors. *Mater. Today* **2020**, *36*, 158–179.
[8] Anasori, B.; Lukatskaya, M. R.; Gogotsi, Y. 2D metal carbides and nitrides (MXenes) for energy storage. *Nat. Rev. Mater.* **2017**, *2*, 16098.
[9] Reina, A.; Jia, X. T.; Ho, J.; Nezich, D.; Son, H.; Bulovic, V.; Dresselhaus, M. S.; Kong, J. Large area, few-layer graphene films on arbitrary substrates by chemical vapor deposition. *Nano Lett.* **2009**, *9*, 30–35.
[10] Kim, J. E.; Oh, J. H.; Kotal, M.; Koratkar, N.; Oh, I. K. Self-assembly and morphological control of three-dimensional macroporous architectures built of two-dimensional materials. *Nano Today* **2017**, *14*, 100–123.
[11] Dillon, A. D.; Ghidiu, M. J.; Krick, A. L.; Griggs, J.; May, S. J.; Gogotsi, Y.; Barsoum, M. W.; Fafarman, A. T. Highly conductive optical quality solution-processed films of 2D titanium carbide. *Adv. Funct. Mater.* **2016**, *26*, 4162–4168.
[12] Lipatov, A.; Alhabeb, M.; Lukatskaya, M. R.; Boson, A.; Gogotsi, Y.; Sinitskii, A. Effect of synthesis on quality, electronic properties and environmental stability of individual monolayer Ti_3C_2 MXene flakes. *Adv. Electron. Mater.* **2016**, *2*, 1600255.
[13] Zhang, C. J.; Anasori, B.; Seral-Ascaso, A.; Park, S. H.; McEvoy, N.; Shmeliov, A.; Duesberg, G. S.; Coleman, J. N.; Gogotsi, Y.; Nicolosi, V. Transparent, flexible, and conductive 2D titanium carbide (MXene) films with high volumetric capacitance. *Adv. Mater.* **2017**, *29*, 1702678.
[14] Zhang, L.; Alvarez, N. T.; Zhang, M. X.; Haase, M.; Malik, R.; Mast, D.; Shanov, V. Preparation and characterization of graphene paper for electromagnetic interference shielding. *Carbon* **2015**, *82*, 353–359.
[15] Shen, B.; Zhai, W. T.; Zheng, W. G. Ultrathin flexible graphene film: An excellent thermal conducting material with efficient EMI shielding. *Adv. Funct. Mater.* **2014**, *24*, 4542–4548.
[16] Liu, J.; Zhang, H. B.; Sun, R. H.; Liu, Y. F.; Liu, Z. S.; Zhou, A. G.; Yu, Z. Z. Hydrophobic, flexible, and lightweight MXene foams for high-performance electromagnetic-interference shielding. *Adv. Mater.* **2017**, *29*, 1702367.
[17] Hsiao, S. T.; Ma, C. C. M.; Liao, W. H.; Wang, Y. S.; Li, S. M.; Huang, Y. C.; Yang, R. B.; Liang, W. F. Lightweight and flexible reduced graphene oxide/water-borne polyurethane composites with high electrical conductivity and excellent electromagnetic interference shielding performance. *ACS Appl. Mater. Interfaces* **2014**, *6*, 10667–10678.
[18] Hong, S. K.; Kim, K. Y.; Kim, T. Y.; Kim, J. H.; Park, S. W.; Kim, J. H.; Cho, B. J. Electromagnetic interference shielding effectiveness of monolayer graphene. *Nanotechnology* **2012**, *23*, 455704.
[19] He, Q. M.; Tao, J. R.; Yang, Y.; Yang, D.; Zhang, K.; Fei, B.; Wang, M. Electric-magnetic-dielectric synergism and salisbury screen effect in laminated polymer composites with multiwall carbon nanotube, nickel, and antimony trioxide for enhancing electromagnetic interference shielding. *Compos. Part A: Appl. Sci. Manuf.* **2022**, *156*, 106901.
[20] Yang, Y.; Tao, J. R.; Yang, D.; He, Q. M.; Chen, X. D.; Wang, M. Improving dispersion and delamination of graphite in biodegradable starch materials via constructing cation-π interaction: Towards microwave shielding enhancement. *J. Mater. Sci. Technol.* **2022**, *129*, 196–205.
[21] Cai, J. H.; Tang, X. H.; Chen, X. D.; Wang, M. Temperature and strain-induced tunable electromagnetic interference shielding in polydimethylsiloxane/multi-walled carbon nanotube composites with temperature-sensitive microspheres. *Compos. Part A: Appl. Sci. Manuf.* **2021**, *140*, 106188.
[22] Gao, Y. N.; Wang, Y.; Yue, T. N.; Zhao, B.; Che, R. C.; Wang, M. Superstructure silver micro-tube composites for ultrahigh electromagnetic wave shielding. *Chem. Eng. J.* **2022**, *430*, 132949.
[23] Shen, X.; Zheng, Q. B.; Kim, J. K. Rational design of two-dimensional nanofillers for polymer nanocomposites toward multifunctional applications. *Prog. Mater. Sci.* **2021**, *115*, 100708.
[24] Zhao, B.; Hamidinejad, M.; Wang, S.; Bai, P. W.; Che, R. C.; Zhang, R.; Park, C. B. Advances in electromagnetic shielding properties of composite foams. *J. Mater. Chem. A* **2021**, *9*, 8896–8949.
[25] Han, M. K.; Shuck, C. E.; Rakhmanov, R.; Parchment, D.; Anasori, B.; Koo, C. M.; Friedman, G.; Gogotsi, Y. Beyond $Ti_3C_2T_x$: MXenes for electromagnetic interference shielding. *ACS Nano* **2020**, *14*, 5008–5016.
[26] Tan, X.; Yuan, Q. L.; Qiu, M. T.; Yu, J. H.; Jiang, N.; Lin, C. T.; Dai, W. Rational design of graphene/polymer composites with excellent electromagnetic interference shielding effectiveness and high thermal conductivity: A mini review. *J. Mater. Sci. Technol.* **2022**, *117*, 238–250.
[27] Iqbal, A.; Sambyal, P.; Koo, C. M. 2D MXenes for electromagnetic shielding: A review. *Adv. Funct. Mater.* **2020**, *30*, 2000883.
[28] Wang, L.; Ma, Z. L.; Zhang, Y. L.; Chen, L. X.; Cao, D. P.; Gu, J. W. Polymer-based EMI shielding composites with 3D conductive networks: A mini-review. *SusMat* **2021**, *1*, 413–431.
[29] Wang, M.; Tang, X. H.; Cai, J. H.; Wu, H.; Shen, J. B.; Guo, S. Y. Construction, mechanism and prospective of conductive polymer composites with multiple interfaces for electromagnetic interference shielding: A review. *Carbon* **2021**, *177*, 377–402.
[30] Qin, M.; Zhang, L. M.; Wu, H. J. Dielectric loss mechanism in electromagnetic wave absorbing materials. *Adv. Sci.* **2022**, *9*, 2105553.
[31] Wang, X. X.; Cao, W. Q.; Cao, M. S.; Yuan, J. Assembling nano-microarchitecture for electromagnetic absorbers and smart devices. *Adv. Mater.* **2020**, *32*, 2002112.
[32] Song, Q.; Ye, F.; Kong, L.; Shen, Q. L.; Han, L. Y.; Feng, L.; Yu, G. J.; Pan, Y. A.; Li, H. J. Graphene and MXene nanomaterials: Toward high-performance electromagnetic wave absorption in gigahertz band range. *Adv. Funct. Mater.* **2020**, *30*, 2000475.
[33] Shu, J. C.; Cao, W. Q.; Cao, M. S. Diverse metal-organic framework architectures for electromagnetic absorbers and shielding. *Adv. Funct. Mater.* **2021**, *31*, 2100470.
[34] Zhang, Y.; Xu, M. K.; Wang, Z. G.; Zhao, T. Y.; Liu, L. X.; Zhang, H. B.; Yu, Z. Z. Strong and conductive reduced graphene oxide-MXene porous films for efficient electromagnetic interference shielding. *Nano Res.* **2022**, *15*, 4916–4924.
[35] Wu, Y.; Wang, Z. Y.; Liu, X.; Shen, X.; Zheng, Q. B.; Xue, Q.; Kim, J. K. Ultralight graphene foam/conductive polymer composites for exceptional electromagnetic interference shielding. *ACS Appl. Mater. Interfaces* **2017**, *9*, 9059–9069.
[36] Zeng, Z. H.; Wang, C. X.; Siqueira, G.; Han, D. X.; Huch, A.; Abdolhosseinzadeh, S.; Heier, J.; Nüesch, F.; Zhang, C. F.; Nyström, G. Nanocellulose-MXene biomimetic aerogels with orientation-tunable electromagnetic interference shielding performance. *Adv. Sci.* **2020**, *7*, 2000979.
[37] Yu, Y. H.; Yi, P.; Xu, W. B.; Sun, X.; Deng, G.; Liu, X. F.; Shui, J. L.; Yu, R. H. Environmentally tough and stretchable MXene organohydrogel with exceptionally enhanced electromagnetic interference shielding performances. *Nano-Micro Lett.* **2022**, *14*, 77.
[38] Liu, J.; Mckeon, L.; Garcia, J.; Pinilla, S.; Barwich, S.; Möbius, M.; Stamenov, P.; Coleman, J. N.; Nicolosi, V. Additive manufacturing

of Ti_3C_2-MXene-functionalized conductive polymer hydrogels for electromagnetic-interference shielding. *Adv. Mater.* **2022**, *34*, 2106253.

[39] Sun, X. Y.; Liu, X.; Shen, X.; Wu, Y.; Wang, Z. Y.; Kim, J. K. Graphene foam/carbon nanotube/poly(dimethyl siloxane) composites for exceptional microwave shielding. *Compos. Part A: Appl. Sci. Manuf.* **2016**, *85*, 199–206.

[40] Fang, H. M.; Guo, H. C.; Hu, Y. R.; Ren, Y. J.; Hsu, P. C.; Bai, S. L. *In-situ* grown hollow Fe_3O_4 onto graphene foam nanocomposites with high EMI shielding effectiveness and thermal conductivity.. *Compos. Sci. Technol.* **2020**, *188*, 107975.

[41] Shui, X. P.; Chung, D. D. L. Nickel filament polymer-matrix composites with low surface impedance and high electromagnetic interference shielding effectiveness. *J. Electron. Mater.* **1997**, *26*, 928–934.

[42] Wu, Y.; Lin, X. Y.; Shen, X.; Sun, X. Y.; Liu, X.; Wang, Z. Y.; Kim, J. K. Exceptional dielectric properties of chlorine-doped graphene oxide/poly(vinylidene fluoride) nanocomposites. *Carbon* **2015**, *89*, 102–112.

[43] Wang, Z. Y.; Han, N. M.; Wu, Y.; Liu, X.; Shen, X.; Zheng, Q. B.; Kim, J. K. Ultrahigh dielectric constant and low loss of highly-aligned graphene aerogel/poly(vinyl alcohol) composites with insulating barriers. *Carbon* **2017**, *123*, 385–394.

[44] Wu, Y.; Wang, Z. Y.; Shen, X.; Liu, X.; Han, N. M.; Zheng, Q. B.; Mai, Y. W.; Kim, J. K. Graphene/boron nitride-polyurethane microlaminates for exceptional dielectric properties and high energy densities. *ACS Appl. Mater. Interfaces* **2018**, *10*, 26641–26652.

[45] Tu, S. B.; Jiang, Q.; Zhang, X. X.; Alshareef, H. N. Large dielectric constant enhancement in MXene percolative polymer composites. *ACS Nano* **2018**, *12*, 3369–3377.

[46] Guo, F. M.; Shen, X.; Zhou, J. M.; Liu, D.; Zheng, Q. B.; Yang, J. L.; Jia, B. H.; Lau, A. K. T.; Kim, J. K. Highly thermally conductive dielectric nanocomposites with synergistic alignments of graphene and boron nitride nanosheets. *Adv. Funct. Mater.* **2020**, *30*, 1910826.

[47] He, Z. Z.; Yu, X.; Yang, J. H.; Zhang, N.; Huang, T.; Wang, Y.; Zhou, Z. W. Largely enhanced dielectric properties of poly(vinylidene fluoride) composites achieved by adding polypyrrole-decorated graphene oxide. *Compos. Part A: Appl. Sci. Manuf.* **2018**, *104*, 89–100.

[48] Liang, C. B.; Song, P.; Qiu, H.; Zhang, Y. L.; Ma, X. T.; Qi, F. Q.; Gu, H. B.; Kong, J.; Cao, D. P.; Gu, J. W. Constructing interconnected spherical hollow conductive networks in silver platelets/reduced graphene oxide foam/epoxy nanocomposites for superior electromagnetic interference shielding effectiveness. *Nanoscale* **2019**, *11*, 22590–22598.

[49] Lin, X. Y.; Shen, X.; Zheng, Q. B.; Yousefi, N.; Ye, L.; Mai, Y. W.; Kim, J. K. Fabrication of highly-aligned, conductive, and strong graphene papers using ultralarge graphene oxide sheets. *ACS Nano* **2012**, *6*, 10708–10719.

[50] Shen, X.; Wang, Z. Y.; Wu, Y.; Liu, X.; He, Y. B.; Zheng, Q. B.; Yang, Q. H.; Kang, F. Y.; Kim, J. K. A three-dimensional multilayer graphene web for polymer nanocomposites with exceptional transport properties and fracture resistance. *Mater. Horiz.* **2018**, *5*, 275–284.

[51] Ji, K. J.; Zhao, H. H.; Zhang, J.; Chen, J.; Dai, Z. D. Fabrication and electromagnetic interference shielding performance of open-cell foam of a Cu-Ni alloy integrated with CNTs. *Appl. Surf. Sci.* **2014**, *311*, 351–356.

[52] Shen, X.; Kim, J. K. Building 3D architecture in 2D thin film for effective EMI shielding. *Matter* **2019**, *1*, 796–798.

[53] Huang, M.; Wang, C. H.; Quan, L.; Nguyen, T. H. Y.; Zhang, H. Y.; Jiang, Y.; Byun, G.; Ruoff, R. S. CVD growth of porous graphene foam in film form. *Matter* **2020**, *3*, 487–497.

[54] Kashani, H.; Giroux, M.; Johnson, I.; Han, J. H.; Wang, C.; Chen, M. W. Unprecedented electromagnetic interference shielding from three-dimensional Bi-continuous nanoporous graphene. *Matter* **2019**, *1*, 1077–1087.

[55] Kim, E.; Zhang, H. M.; Lee, J. H.; Chen, H. M.; Zhang, H.; Javed, M. H.; Shen, X.; Kim, J. K. MXene/polyurethane auxetic composite foam for electromagnetic interference shielding and impact attenuation. *Compos. Part A: Appl. Sci. Manuf.* **2021**, *147*, 106430.

[56] Fan, D. L.; Li, N. X.; Li, M. G.; Wang, S.; Li, S. X.; Tang, T. Polyurethane/polydopamine/graphene auxetic composite foam with high-efficient and tunable electromagnetic interference shielding performance. *Chem. Eng. J.* **2022**, *427*, 131635.

[57] Zhang, Y. L.; Yan, Y.; Qiu, H.; Ma, Z. L.; Ruan, K. P.; Gu, J. W. A mini-review of MXene porous films: Preparation, mechanism and application. *J. Mater. Sci. Technol.* **2022**, *103*, 42–49.

[58] Sun, R. H.; Zhang, H. B.; Liu, J.; Xie, X.; Yang, R.; Li, Y.; Hong, S.; Yu, Z. Z. Highly conductive transition metal carbide/carbonitride(MXene)@polystyrene nanocomposites fabricated by electrostatic assembly for highly efficient electromagnetic interference shielding. *Adv. Funct. Mater.* **2017**, *27*, 1702807.

[59] Zhao, M. Q.; Xie, X. Q.; Ren, C. E.; Makaryan, T.; Anasori, B.; Wang, G. X.; Gogotsi, Y. Hollow MXene spheres and 3D macroporous MXene frameworks for Na-ion storage. *Adv. Mater.* **2017**, *29*, 1702410.

[60] Li, X. F.; Tao, Z. C.; Hao, B. Y.; Kong, Q. Q.; Liu, Z.; Liu, Z. J.; Guo, Q. G.; Liu, L. Reduced graphene oxide bubbles with tunable electromagnetic shielding effectiveness. *Scr. Mater.* **2020**, *187*, 407–412.

[61] Wang, X. H.; Chen, Y. Q.; Hu, F. Y.; Zhang, S.; Fan, B. B.; Min, Z. Y.; Zhang, R.; Zhao, B.; Wang, H. L.; Lu, H. X. et al. Electromagnetic interference shielding performance of flexible, hydrophobic honeycomb-structured Ag@$Ti_3C_2T_x$ composites. *Adv. Electron. Mater.* **2022**, *8*, 2101028.

[62] Chen, Q. Q.; Fan, B. B.; Zhang, Q. P.; Wang, S.; Cui, W.; Jia, Y. C.; Xu, S. K.; Zhao, B.; Zhang, R. Design of 3D lightweight $Ti_3C_2T_x$ MXene porous film with graded holes for efficient electromagnetic interference shielding performance. *Ceram. Int.* **2022**, *48*, 14578–14586.

[63] Liu, X.; Sun, X. Y.; Wang, Z. Y.; Shen, X.; Wu, Y.; Kim, J. K. Planar porous graphene woven fabric/epoxy composites with exceptional electrical, mechanical properties, and fracture toughness. *ACS Appl. Mater. Interfaces* **2015**, *7*, 21455–21464.

[64] Jia, J. J.; Sun, X. Y.; Lin, X. Y.; Shen, X.; Mai, Y. W.; Kim, J. K. Exceptional electrical conductivity and fracture resistance of 3D interconnected graphene foam/epoxy composites. *ACS Nano* **2014**, *8*, 5774–5783.

[65] Shi, M. K.; Shen, M. M.; Guo, X. Y.; Jin, X. X.; Cao, Y. X.; Yang, Y. Y.; Wang, W. J.; Wang, J. F. $Ti_3C_2T_x$ MXene-decorated nanoporous polyethylene textile for passive and active personal precision heating. *ACS Nano* **2021**, *15*, 11396–11405.

[66] Ling, Z.; Ren, C. E.; Zhao, M. Q.; Yang, J.; Giammarco, J. M.; Qiu, J. S.; Barsoum, M. W.; Gogotsi, Y. Flexible and conductive MXene films and nanocomposites with high capacitance. *Proc. Natl. Acad. Sci. USA* **2014**, *111*, 16676–16681.

[67] Luo, J. M.; Tao, X. Y.; Zhang, J.; Xia, Y.; Huang, H.; Zhang, L. Y.; Gan, Y. P.; Liang, C.; Zhang, W. K. Sn^{4+} ion decorated highly conductive Ti_3C_2 MXene: Promising lithium-ion anodes with enhanced volumetric capacity and cyclic performance. *ACS Nano* **2016**, *10*, 2491–2499.

[68] Liu, W. H.; Wang, Z. Q.; Su, Y. L.; Li, Q. W.; Zhao, Z. G.; Geng, F. X. Molecularly stacking manganese dioxide/titanium carbide sheets to produce highly flexible and conductive film electrodes with improved pseudocapacitive performances. *Adv. Energy Mater.* **2017**, *7*, 1602834.

[69] Boota, M.; Anasori, B.; Voigt, C.; Zhao, M. Q.; Barsoum, M. W.; Gogotsi, Y. Pseudocapacitive electrodes produced by oxidant-free polymerization of pyrrole between the layers of 2D titanium carbide (MXene). *Adv. Mater.* **2016**, *28*, 1517–1522.

[70] Shao, Y. L.; El-Kady, M. F.; Lin, C. W.; Zhu, G. Z.; Marsh, K. L.; Hwang, J. Y.; Zhang, Q. H.; Li, Y. G.; Wang, H. Z.; Kaner, R. B. 3D freeze-casting of cellular graphene films for ultrahigh-power-density supercapacitors. *Adv. Mater.* **2016**, *28*, 6719–6726.

[71] Zhou, Z. H.; Liu, J. Z.; Zhang, X. X.; Tian, D.; Zhan, Z. Y.; Lu, C. H. Ultrathin MXene/calcium alginate aerogel film for high-performance electromagnetic interference shielding. *Adv. Mater. Interfaces* **2019**, *6*, 1802040.

[72] Ma, Z. Y.; Zhou, X. F.; Deng, W.; Lei, D.; Liu, Z. P. 3D porous

MXene (Ti_3C_2)/reduced graphene oxide hybrid films for advanced lithium storage. *ACS Appl. Mater. Interfaces* **2018**, *10*, 3634–3643.
[73] Zhang, Y. L.; Ruan, K. P.; Shi, X. T.; Qiu, H.; Pan, Y.; Yan, Y.; Gu, J. W. $Ti_3C_2T_x$/RGO porous composite films with superior electromagnetic interference shielding performances. *Carbon* **2021**, *175*, 271–280.
[74] Lai, D. G.; Chen, X. X.; Wang, Y. Controllable fabrication of elastomeric and porous graphene films with superior foldable behavior and excellent electromagnetic interference shielding performance. *Carbon* **2020**, *158*, 728–737.
[75] Xu, J. D.; Chang, H.; Zhao, B. C.; Li, R. S.; Cui, T. M.; Jian, J.; Yang, Y.; Tian, H.; Zhang, S.; Ren, T. L. Highly stretchable and conformal electromagnetic interference shielding armor with strain sensing ability. *Chem. Eng. J.* **2022**, *431*, 133908.
[76] El-Kady, M. F.; Strong, V.; Dubin, S.; Kaner, R. B. Laser scribing of high-performance and flexible graphene-based electrochemical capacitors. *Science* **2012**, *335*, 1326–1330.
[77] Yin, L.; Kang, H.; Ma, H. X.; Wang, J. F.; Liu, Y. Y.; Xie, Z. M.; Wang, Y. S.; Fan, Z. M. Sunshine foaming of compact $Ti_3C_2T_x$ MXene film for highly efficient electromagnetic interference shielding and energy storage. *Carbon* **2021**, *182*, 124–133.
[78] Shen, B.; Li, Y.; Yi, D.; Zhai, W. T.; Wei, X. C.; Zheng, W. G. Microcellular graphene foam for improved broadband electromagnetic interference shielding. *Carbon* **2016**, *102*, 154–160.
[79] Weng, C. X.; Wang, G. R.; Dai, Z. H.; Pei, Y. M.; Liu, L. Q.; Zhang, Z. Buckled AgNW/MXene hybrid hierarchical sponges for high-performance electromagnetic interference shielding. *Nanoscale* **2019**, *11*, 22804–22812.
[80] Zeng, Z. H.; Wu, N.; Wei, J. J.; Yang, Y. F.; Wu, T. T.; Li, B.; Hauser, S. B.; Yang, W. D.; Liu, J. R.; Zhao, S. Y. Porous and ultra-flexible crosslinked MXene/polyimide composites for multifunctional electromagnetic interference shielding. *Nano-Micro Lett.* **2022**, *14*, 59.
[81] Shen, B.; Li, Y.; Zhai, W. T.; Zheng, W. G. Compressible graphene-coated polymer foams with ultralow density for adjustable electromagnetic interference (EMI) shielding. *ACS Appl. Mater. Interfaces* **2016**, *8*, 8050–8057.
[82] Fu, B. Q.; Ren, P. G.; Guo, Z. Z.; Du, Y. L.; Jin, Y. L.; Sun, Z. F.; Dai, Z.; Ren, F. Construction of three-dimensional interconnected graphene nanosheet network in thermoplastic polyurethane with highly efficient electromagnetic interference shielding. *Compos. Part B:Eng.* **2021**, *215*, 108813.
[83] Cheng, H. R.; Xing, L. L.; Zuo, Y.; Pan, Y. M.; Huang, M. N.; Alhadhrami, A.; Ibrahim, M. M.; El-Bahy, Z. M.; Liu, C. T.; Shen, C. Y. et al. Constructing nickel chain/MXene networks in melamine foam towards phase change materials for thermal energy management and absorption-dominated electromagnetic interference shielding. *Adv. Compos. Hybrid Mater.* **2022**, *5*, 755–765.
[84] Ma, W. J.; Cai, W. R.; Chen, W. H.; Liu, P. J.; Wang, J. F.; Liu, Z. X. A novel structural design of shielding capsule to prepare high-performance and self-healing MXene-based sponge for ultra-efficient electromagnetic interference shielding. *Chem. Eng. J.* **2021**, *426*, 130729.
[85] Li, X. S.; Cai, W. W.; An, J.; Kim, S.; Nah, J.; Yang, D. X.; Piner, R.; Velamakanni, A.; Jung, I.; Tutuc, E. et al. Large-area synthesis of high-quality and uniform graphene films on copper foils. *Science* **2009**, *324*, 1312–1314.
[86] Chen, Z. P.; Ren, W. C.; Gao, L. B.; Liu, B. L.; Pei, S. F.; Cheng, H. M. Three-dimensional flexible and conductive interconnected graphene networks grown by chemical vapour deposition. *Nat. Mater.* **2011**, *10*, 424–428.
[87] Nguyen, V. T.; Min, B. K.; Yi, Y.; Kim, S. J.; Choi, C. G. MXene($Ti_3C_2T_x$)/graphene/PDMS composites for multifunctional broadband electromagnetic interference shielding skins. *Chem. Eng. J.* **2020**, *393*, 124608.
[88] Kong, L.; Yin, X. W.; Han, M. K.; Yuan, X. Y.; Hou, Z. X.; Ye, F.; Zhang, L. T.; Cheng, L. F.; Xu, Z. W.; Huang, J. F. Macroscopic bioinspired graphene sponge modified with *in-situ* grown carbon nanowires and its electromagnetic properties. *Carbon* **2017**, *111*, 94–102.
[89] Yang, Y. L.; Zuo, Y.; Feng, L.; Hou, X. J.; Suo, G. Q.; Ye, X. H.; Zhang, L. Powerful and lightweight electromagnetic-shielding carbon nanotube/graphene foam/silicon carbide composites. *Mater. Lett.* **2019**, *256*, 126634.
[90] Shao, G. F.; Hanaor, D. A. H.; Shen, X. D.; Gurlo, A. Freeze casting: From low-dimensional building blocks to aligned porous structures—A review of novel materials, methods, and applications. *Adv. Mater.* **2020**, *32*, 1907176.
[91] Zhao, S.; Zhang, H. B.; Luo, J. Q.; Wang, Q. W.; Xu, B.; Hong, S.; Yu, Z. Z. Highly electrically conductive three-dimensional $Ti_3C_2T_x$ MXene/reduced graphene oxide hybrid aerogels with excellent electromagnetic interference shielding performances. *ACS Nano* **2018**, *12*, 11193–11202.
[92] Yang, J.; Yang, W.; Chen, W.; Tao, X. M. An elegant coupling: Freeze-casting and versatile polymer composites. *Prog. Polym. Sci.* **2020**, *109*, 101289.
[93] Yang, J.; Chan, K. Y.; Venkatesan, H.; Kim, E.; Adegun, M. H.; Lee, J. H.; Shen, X.; Kim, J. K. Superinsulating BNNS/PVA composite aerogels with high solar reflectance for energy-efficient buildings. *Nano-Micro Lett.* **2022**, *14*, 54.
[94] Zhang, H. M.; Shen, X.; Kim, E.; Wang, M. Y.; Lee, J. H.; Chen, H. M.; Zhang, G. C.; Kim, J. K. Integrated water and thermal managements in bioinspired hierarchical MXene aerogels for highly efficient solar-powered water evaporation. *Adv. Funct. Mater.* **2022**, *32*, 2111794.
[95] Wang, Z. Y.; Shen, X.; Han, N. M.; Liu, X.; Wu, Y.; Ye, W. J.; Kim, J. K. Ultralow electrical percolation in graphene aerogel/epoxy composites. *Chem. Mater.* **2016**, *28*, 6731–6741.
[96] Wang, C. H.; Chen, X.; Wang, B.; Huang, M.; Wang, B.; Jiang, Y.; Ruoff, R. S. Freeze-casting produces a graphene oxide aerogel with a radial and centrosymmetric structure. *ACS Nano* **2018**, *12*, 5816–5825.
[97] Xu, W. Z.; Xing, Y.; Liu, J.; Wu, H. P.; Cui, Y.; Li, D. W.; Guo, D. Y.; Li, C. R.; Liu, A. P.; Bai, H. Efficient water transport and solar steam generation via radially, hierarchically structured aerogels. *ACS Nano* **2019**, *13*, 7930–7938.
[98] Bian, R. J.; He, G. L.; Zhi, W. Q.; Xiang, S. L.; Wang, T. W.; Cai, D. Y. Ultralight MXene-based aerogels with high electromagnetic interference shielding performance. *J. Mater. Chem. C* **2019**, *7*, 474–478.
[99] Han, M. K.; Yin, X. W.; Hantanasirisakul, K.; Li, X. L.; Iqbal, A.; Hatter, C. B.; Anasori, B.; Koo, C. M.; Torita, T.; Soda, Y. et al. Anisotropic MXene aerogels with a mechanically tunable ratio of electromagnetic wave reflection to absorption. *Adv. Opt. Mater.* **2019**, *7*, 1900267.
[100] Tetik, H.; Orangi, J.; Yang, G.; Zhao, K. R.; Mujib, S. B.; Singh, G.; Beidaghi, M.; Lin, D. 3D printed MXene aerogels with truly 3D macrostructure and highly engineered microstructure for enhanced electrical and electrochemical performance. *Adv. Mater.* **2022**, *34*, 2104980.
[101] Cong, H. P.; Wang, P.; Yu, S. H. Stretchable and self-healing graphene oxide-polymer composite hydrogels: A dual-network design. *Chem. Mater.* **2013**, *25*, 3357–3362.
[102] Shang, T. X.; Lin, Z. F.; Qi, C. S.; Liu, X. C.; Li, P.; Tao, Y.; Wu, Z. T.; Li, D. W.; Simon, P.; Yang, Q. H. 3D Macroscopic architectures from self-assembled MXene hydrogels. *Adv. Funct. Mater.* **2019**, *29*, 1903960.
[103] Li, C.; Shi, G. Q. Functional gels based on chemically modified graphenes. *Adv. Mater.* **2014**, *26*, 3992–4012.
[104] Wang, M.; Duan, X. D.; Xu, Y. X.; Duan, X. F. Functional three-dimensional graphene/polymer composites. *ACS Nano* **2016**, *10*, 7231–7247.
[105] Xu, Y. X.; Sheng, K. X.; Li, C.; Shi, G. Q. Self-assembled graphene hydrogel via a one-step hydrothermal process. *ACS Nano* **2010**, *4*, 4324–4330.
[106] Wang, Z. Y.; Shen, X.; Akbari Garakani, M.; Lin, X. Y.; Wu, Y.; Liu, X.; Sun, X. Y.; Kim, J. K. Graphene aerogel/epoxy composites with exceptional anisotropic structure and properties. *ACS Appl. Mater. Interfaces* **2015**, *7*, 5538–5549.
[107] Lai, D. G.; Chen, X. X.; Wang, G.; Xu, X. H.; Wang, Y. Arbitrarily reshaping and instantaneously self-healing graphene composite hydrogel with molecule polarization-enhanced ultrahigh

electromagnetic interference shielding performance. *Carbon* **2022**, *188*, 513–522.
[108] Yang, W. X.; Shao, B. W.; Liu, T. Y.; Zhang, Y. Y.; Huang, R.; Chen, F.; Fu, Q. Robust and mechanically and electrically self-healing hydrogel for efficient electromagnetic interference shielding. *ACS Appl. Mater. Interfaces* **2018**, *10*, 8245–8257.
[109] Zhu, Y. Y.; Liu, J.; Guo, T.; Wang, J. J.; Tang, X. Z.; Nicolosi, V. Multifunctional $Ti_3C_2T_x$ MXene Composite hydrogels with strain sensitivity toward absorption-dominated electromagnetic-interference shielding. *ACS Nano* **2021**, *15*, 1465–1474.
[110] Zhou, C. X.; Yuan, S. W.; Dai, T. W.; Zhou, S. T.; Zou, H. W.; Liu, P. B. Environment-adaptable PAM/PVA semi-IPN hydrogels reinforced by GO for high electromagnetic shielding performance. *Polymer* **2022**, *253*, 125028.
[111] Dai, Y.; Wu, X. Y.; Li, L. L.; Zhang, Y.; Deng, Z. M.; Yu, Z. Z.; Zhang, H. B. 3D Printing of resilient, lightweight and conductive MXene/reduced graphene oxide architectures for broadband electromagnetic interference shielding. *J. Mater. Chem. A* **2022**, *10*, 11375–11385.
[112] Ghaffarkhah, A.; Kamkar, M.; Dijvejin, Z. A.; Riazi, H.; Ghaderi, S.; Golovin, K.; Soroush, M.; Arjmand, M. High-resolution extrusion printing of Ti_3C_2-based inks for wearable human motion monitoring and electromagnetic interference shielding. *Carbon* **2022**, *191*, 277–289.
[113] Zhu, C.; Han, T. Y. J.; Duoss, E. B.; Golobic, A. M.; Kuntz, J. D.; Spadaccini, C. M.; Worsley, M. A. Highly compressible 3D periodic graphene aerogel microlattices. *Nat. Commun.* **2015**, *6*, 6962.
[114] Chizari, K.; Arjmand, M.; Liu, Z.; Sundararaj, U.; Therriault, D. Three-dimensional printing of highly conductive polymer nanocomposites for EMI shielding applications. *Mater. Today Commun.* **2017**, *11*, 112–118.
[115] Liu, S. J.; Bastola, A. K.; Li, L. A 3D printable and mechanically robust hydrogel based on alginate and graphene oxide. *ACS Appl. Mater. Interfaces* **2017**, *9*, 41473–41481.
[116] Moyano, J. J.; Gómez-Gómez, A.; Pérez-Coll, D.; Belmonte, M.; Miranzo, P.; Osendi, M. I. Filament printing of graphene-based inks into self-supported 3D architectures. *Carbon* **2019**, *151*, 94–102.
[117] Yao, Y. G.; Fu, K. K.; Yan, C. Y.; Dai, J. Q.; Chen, Y. N.; Wang, Y. B.; Zhang, B. L.; Hitz, E.; Hu, L. B. Three-dimensional printable high-temperature and high-rate heaters. *ACS Nano* **2016**, *10*, 5272–5279.
[118] Gao, T. T.; Yang, Z.; Chen, C. J.; Li, Y. J.; Fu, K.; Dai, J. Q.; Hitz, E. M.; Xie, H.; Liu, B. Y.; Song, J. W. et al. Three-dimensional printed thermal regulation textiles. *ACS Nano* **2017**, *11*, 11513–11520.
[119] Zhang, M. C.; Wang, Y. L.; Jian, M. Q.; Wang, C. Y.; Liang, X. P.; Niu, J. L.; Zhang, Y. Y. Spontaneous alignment of graphene oxide in hydrogel during 3D printing for multistimuli-responsive actuation. *Adv. Sci.* **2020**, *7*, 1903048.
[120] Ling, J. Q.; Zhai, W. T.; Feng, W. W.; Shen, B.; Zhang, J. F.; Zheng, W. G. Facile preparation of lightweight microcellular polyetherimide/graphene composite foams for electromagnetic interference shielding. *ACS Appl. Mater. Interfaces* **2013**, *5*, 2677–2684.
[121] Xia, S. H.; Wei, C. L.; Tang, J. C.; Yan, J. H. Tensile stress-gated electromagnetic interference shielding fabrics with real-time adjustable shielding efficiency. *ACS Sustainable Chem. Eng.* **2021**, *9*, 13999–14005.
[122] Zhu, R. Q.; Li, Z. Y.; Deng, G.; Yu, Y. H.; Shui, J. L.; Yu, R. H.; Pan, C. F.; Liu, X. F. Anisotropic magnetic liquid metal film for wearable wireless electromagnetic sensing and smart electromagnetic interference shielding. *Nano Energy* **2022**, *92*, 106700.
[123] Wen, B.; Cao, M. S.; Lu, M. M.; Cao, W. Q.; Shi, H. L.; Liu, J.; Wang, X. X.; Jin, H. B.; Fang, X. Y.; Wang, W. Z. et al. Reduced graphene oxides: Light-weight and high-efficiency electromagnetic interference shielding at elevated temperatures. *Adv. Mater.* **2014**, *26*, 3484–3489.
[124] Cao, M. S.; Wang, X. X.; Cao, W. Q.; Fang, X. Y.; Wen, B.; Yuan, J. Thermally driven transport and relaxation switching self-powered electromagnetic energy conversion. *Small* **2018**, *14*, 1800987.
[125] Lv, H. L.; Yang, Z. H.; Ong, S. J. H.; Wei, C.; Liao, H. B.; Xi, S. B.; Du, Y. H.; Ji, G. B.; Xu, Z. J. A flexible microwave shield with tunable frequency-transmission and electromagnetic compatibility. *Adv. Funct. Mater.* **2019**, *29*, 1900163.
[126] Wang, Y. N.; Cheng, X. D.; Song, W. L.; Ma, C. J.; Bian, X. M.; Chen, M. J. Hydro-sensitive sandwich structures for self-tunable smart electromagnetic shielding. *Chem. Eng. J.* **2018**, *344*, 342–352.
[127] Liu, X. F.; Li, Y.; Sun, X.; Tang, W. K.; Deng, G.; Liu, Y. J.; Song, Z. M.; Yu, Y. H.; Yu, R. H.; Dai, L. M. et al. Off/on switchable smart electromagnetic interference shielding aerogel. *Matter* **2021**, *4*, 1735–1747.
[128] Zhu, M.; Yan, X. X.; Xu, H. L.; Xu, Y. J.; Kong, L. Ultralight, compressible, and anisotropic MXene@wood nanocomposite aerogel with excellent electromagnetic wave shielding and absorbing properties at different directions. *Carbon* **2021**, *182*, 806–814.
[129] Chen, J. L.; Shen, B.; Jia, X. C.; Liu, Y. F.; Zheng, W. G. Lightweight and compressible anisotropic honeycomb-like graphene composites for highly tunable electromagnetic shielding with multiple functions. *Mater. Today Phys.* **2022**, *24*, 100695.
[130] Li, H. L.; Jing, L.; Ngoh, Z. L.; Tay, R. Y.; Lin, J. J.; Wang, H.; Tsang, S. H.; Teo, E. H. T. Engineering of high-density thin-layer graphite foam-based composite architectures with superior compressibility and excellent electromagnetic interference shielding performance. *ACS Appl. Mater. Interfaces* **2018**, *10*, 41707–41716.
[131] Wu, X. Y.; Han, B. Y.; Zhang, H. B.; Xie, X.; Tu, T. X.; Zhang, Y.; Dai, Y.; Yang, R.; Yu, Z. Z. Compressible, durable and conductive polydimethylsiloxane-coated MXene foams for high-performance electromagnetic interference shielding. *Chem. Eng. J.* **2020**, *381*, 122622.
[132] Jia, X. C.; Shen, B.; Zhang, L. H.; Zheng, W. G. Construction of compressible polymer/MXene composite foams for high-performance absorption-dominated electromagnetic shielding with ultra-low reflectivity. *Carbon* **2021**, *173*, 932–940.
[133] Yang, B. Q.; Dai, K. R.; Bi, L.; Zhang, W. L.; Li, C. S.; Zhang, J. M.; Yu, D.; Wang, J.; Zhang, H. Superior electromagnetic shielding and mechanical buffering achieved by alternating conductive and porous supramolecular networks. *Adv. Eng. Mater.* **2022**, *24*, 2101511.
[134] Zhang, Y.; Fang, X. X.; Wen, B. Y. Asymmetric Ni/PVC films for high-performance electromagnetic interference shielding. *Chin. J. Polym. Sci.* **2015**, *33*, 899–907.
[135] Wang, H. Y.; Li, T. T.; Wu, L. W.; Lou, C. W.; Lin, J. H. Multifunctional, polyurethane-based foam composites reinforced by a fabric structure: Preparation, mechanical, acoustic, and EMI shielding properties. *Materials* **2018**, *11*, 2085.
[136] Mei, H.; Lu, M. Y.; Zhou, S. X.; Cheng, L. F. Enhanced impact resistance and electromagnetic interference shielding of carbon nanotubes films composites. *J. Appl. Polym. Sci.* **2021**, *138*, 50033.
[137] Yang, W.; Bai, H. X.; Jiang, B.; Wang, C. N.; Ye, W. M.; Li, Z. X.; Xu, C.; Wang, X. B.; Li, Y. F. Flexible and densified graphene/waterborne polyurethane composite film with thermal conducting property for high performance electromagnetic interference shielding. *Nano Res.*, in press, https://doi.org/10.1007/s12274-022-4414-3.
[138] Shen, X.; Kim, J. K. 3D graphene and boron nitride structures for nanocomposites with tailored thermal conductivities: Recent advances and perspectives. *Funct. Compos. Struct.* **2020**, *2*, 022001.
[139] Yu, S.; Shen, X.; Kim, J. K. Beyond homogeneous dispersion: Oriented conductive fillers for high κ nanocomposites. *Mater. Horiz.* **2021**, *8*, 3009–3042.
[140] Shen, X.; Wang, Z. Y.; Wu, Y.; Liu, X.; He, Y. B.; Kim, J. K. Multilayer graphene enables higher efficiency in improving thermal conductivities of graphene/epoxy composites. *Nano Lett.* **2016**, *16*, 3585–3593.
[141] Hamidinejad, M.; Salari, M.; Ma, L.; Moghimian, N.; Zhao, B.; Taylor, H. K.; Filleter, T.; Park, C. B. Electrically and thermally graded microcellular polymer/graphene nanoplatelet composite

foams and their EMI shielding properties. *Carbon* **2022**, *187*, 153–164.
[142] Du, Y. Q.; Xu, J.; Fang, J. Y.; Zhang, Y. T.; Liu, X. Y.; Zuo, P. Y.; Zhuang, Q. X. Ultralight, highly compressible, thermally stable MXene/aramid nanofiber anisotropic aerogels for electromagnetic interference shielding. *J. Mater. Chem. A* **2022**, *10*, 6690–6700.
[143] Liu, C.; Wu, W.; Chen, Q. M.; Wang, Y.; Cui, S. F.; Yang, H. 3D expanded graphite frameworks for dual-functional polymer composites with exceptional thermal conductive and electromagnetic interference shielding capabilities. *ACS Appl. Electron. Mater.* **2022**, *4*, 707–717.
[144] Song, P.; Liu, B.; Liang, C. B.; Ruan, K. P.; Qiu, H.; Ma, Z. L.; Guo, Y. Q.; Gu, J. W. Lightweight, flexible cellulose-derived carbon aerogel@reduced graphene oxide/PDMS composites with outstanding EMI shielding performances and excellent thermal conductivities. *Nano-Micro Lett.* **2021**, *13*, 91.
[145] Li, J. C.; Zhao, X. Y.; Wu, W. J.; Ji, X. W.; Lu, Y. L.; Zhang, L. Q. Bubble-templated rGO-graphene nanoplatelet foams encapsulated in silicon rubber for electromagnetic interference shielding and high thermal conductivity. *Chem. Eng. J.* **2021**, *415*, 129054.
[146] Li, R. S.; Ding, L.; Gao, Q.; Zhang, H. M.; Zeng, D.; Zhao, B.; Fan, B. B.; Zhang, R. Tuning of anisotropic electrical conductivity and enhancement of EMI shielding of polymer composite foam via CO_2-assisted delamination and orientation of MXene. *Chem. Eng. J.* **2021**, *415*, 128930.
[147] Deng, Z. M.; Tang, P. P.; Wu, X. Y.; Zhang, H. B.; Yu, Z. Z. Superelastic, ultralight, and conductive $Ti_3C_2T_x$ MXene/acidified carbon nanotube anisotropic aerogels for electromagnetic interference shielding. *ACS Appl. Mater. Interfaces* **2021**, *13*, 20539–20547.
[148] Cheng, Y.; Li, X. Y.; Qin, Y. X.; Fang, Y. T.; Liu, G. L.; Wang, Z. Y.; Matz, J.; Dong, P.; Shen, J. F.; Ye, M. X. Hierarchically porous polyimide/$Ti_3C_2T_x$ film with stable electromagnetic interference shielding after resisting harsh conditions. *Sci. Adv.* **2021**, *7*, eabj1663.
[149] Xia, B. H.; Zhang, X. H.; Jiang, J.; Wang, Y.; Li, T.; Wang, Z. C.; Chen, M. Q.; Liu, T. X.; Dong, W. F. Facile preparation of high strength, lightweight and thermal insulation polyetherimide/$Ti_3C_2T_x$ MXenes/Ag nanoparticles composite foams for electromagnetic interference shielding. *Compos. Commun.* **2022**, *29*, 101028.
[150] Zhang, H. M.; Zhang, G. C.; Gao, Q.; Tang, M.; Ma, Z. L.; Qin, J. B.; Wang, M. Y.; Kim, J. K. Multifunctional microcellular PVDF/Ni-chains composite foams with enhanced electromagnetic interference shielding and superior thermal insulation performance. *Chem. Eng. J.* **2020**, *379*, 122304.
[151] Qi, F. Q.; Wang, L.; Zhang, Y. L.; Ma, Z. L.; Qiu, H.; Gu, J. W. Robust $Ti_3C_2T_x$ MXene/starch derived carbon foam composites for superior EMI shielding and thermal insulation. *Mater. Today Phys.* **2021**, *21*, 100512.
[152] Shi, H. G.; Zhao, H. B.; Liu, B. W.; Wang, Y. Z. Multifunctional flame-retardant melamine-based hybrid foam for infrared stealth, thermal insulation, and electromagnetic interference shielding. *ACS Appl. Mater. Interfaces* **2021**, *13*, 26505–26514.
[153] Shi, Y. Y.; Xiang, Z.; Cai, L.; Pan, F.; Dong, Y. Y.; Zhu, X. J.; Cheng, J.; Jiang, H. J.; Lu, W. Multi-interface assembled N-doped MXene/HCFG/AgNW films for wearable electromagnetic shielding devices with multimodal energy conversion and healthcare monitoring performances. *ACS Nano* **2022**, *16*, 7816–7833.
[154] Hu, D. W.; Wang, S. Q.; Zhang, C.; Yi, P. S.; Jiang, P. K.; Huang, X. Y. Ultrathin MXene-aramid nanofiber electromagnetic interference shielding films with tactile sensing ability withstanding harsh temperatures. *Nano Res.* **2021**, *14*, 2837–2845.
[155] Huang, W. C.; Hu, L. P.; Tang, Y. F.; Xie, Z. J.; Zhang, H. Recent advances in functional 2D MXene-based nanostructures for next-generation devices. *Adv. Funct. Mater.* **2020**, *30*, 2005223.
[156] Chen, Y. A.; Li, Y. H.; Liu, Y.; Chen, P.; Zhang, C. Z.; Qi, H. S. Holocellulose Nanofibril-assisted intercalation and stabilization of $Ti_3C_2T_x$ MXene inks for multifunctional sensing and EMI shielding applications. *ACS Appl. Mater. Interfaces* **2021**, *13*, 36221–36231.
[157] Zhu, S.; Peng, S. P.; Qiang, Z.; Ye, C. H.; Zhu, M. F. Cryogenic-environment resistant, highly elastic hybrid carbon foams for pressure sensing and electromagnetic interference shielding. *Carbon* **2022**, *193*, 258–271.
[158] Dai, Y.; Wu, X. Y.; Liu, Z. S.; Zhang, H. B.; Yu, Z. Z. Highly sensitive, robust and anisotropic MXene aerogels for efficient broadband microwave absorption. *Compos. Part B:Eng.* **2020**, *200*, 108263.
[159] Cheng, Y.; Zhu, W. D.; Lu, X. F.; Wang, C. Lightweight and flexible MXene/carboxymethyl cellulose aerogel for electromagnetic shielding, energy harvest and self-powered sensing. *Nano Energy* **2022**, *98*, 107229.
[160] Xu, J. D.; Li, R. S.; Ji, S. R.; Zhao, B. C.; Cui, T. R.; Tan, X. C.; Gou, G. Y.; Jian, J. M.; Xu, H. K.; Qiao, Y. C. et al. Multifunctional graphene microstructures inspired by honeycomb for ultrahigh performance electromagnetic interference shielding and wearable applications. *ACS Nano* **2021**, *15*, 8907–8918.
[161] Zhou, Z. H.; Panatdasirisuk, W.; Mathis, T. S.; Anasori, B.; Lu, C. H.; Zhang, X. X.; Liao, Z. W.; Gogotsi, Y.; Yang, S. Layer-by-layer assembly of MXene and carbon nanotubes on electrospun polymer films for flexible energy storage. *Nanoscale* **2018**, *10*, 6005–6013.
[162] Hu, L. B.; Pasta, M.; La Mantia, F.; Cui, L. F.; Jeong, S.; Deshazer, H. D.; Choi, J. W.; Han, S. M.; Cui, Y. Stretchable, porous, and conductive energy textiles. *Nano Lett.* **2010**, *10*, 708–714.
[163] Liu, L. X.; Chen, W.; Zhang, H. B.; Wang, Q. W.; Guan, F. L.; Yu, Z. Z. Flexible and multifunctional silk textiles with biomimetic leaf-like MXene/silver nanowire nanostructures for electromagnetic interference shielding, humidity monitoring, and self-derived hydrophobicity. *Adv. Funct. Mater.* **2019**, *29*, 1905197.
[164] Zhang, X. S.; Wang, X. F.; Lei, Z. W.; Wang, L. L.; Tian, M. W.; Zhu, S. F.; Xiao, H.; Tang, X. N.; Qu, L. J. Flexible MXene-decorated fabric with interwoven conductive networks for integrated joule heating, electromagnetic interference shielding, and strain sensing performances. *ACS Appl. Mater. Interfaces* **2020**, *12*, 14459–14467.
[165] Zheng, X. H.; Nie, W. Q.; Hu, Q. L.; Wang, X. W.; Wang, Z. Q.; Zou, L. H.; Hong, X. H.; Yang, H. W.; Shen, J. K.; Li, C. L. Multifunctional RGO/$Ti_3C_2T_x$ MXene fabrics for electrochemical energy storage, electromagnetic interference shielding, electrothermal and human motion detection. *Mater. Des.* **2021**, *200*, 109442.
[166] Zhang, D. B.; Yin, R.; Zheng, Y. J.; Li, Q. M.; Liu, H.; Liu, C. T.; Shen, C. Y. Multifunctional MXene/CNTs based flexible electronic textile with excellent strain sensing, electromagnetic interference shielding and joule heating performances. *Chem. Eng. J.* **2022**, *438*, 135587.
[167] Zheng, X. H.; Wang, P.; Zhang, X. S.; Hu, Q. L.; Wang, Z. Q.; Nie, W. Q.; Zou, L. H.; Li, C. L.; Han, X. Breathable, durable and bark-shaped MXene/textiles for high-performance wearable pressure sensors, EMI shielding and heat physiotherapy. *Compos. Part A: Appl. Sci. Manuf.* **2022**, *152*, 106700.
[168] Simon, R. M. EMI shielding through conductive plastics. *Polym. Plast. Technol. Eng.* **1981**, *17*, 1–10.
[169] Ryu, S. H.; Park, B.; Han, Y. K.; Kwon, S. J.; Kim, T.; Lamouri, R.; Kim, K. H.; Lee, S. B. Electromagnetic wave shielding flexible films with near-zero reflection in the 5G frequency band. *J. Mater. Chem. A* **2022**, *10*, 4446–4455.
[170] Ryu, S. H.; Han, Y. K.; Kwon, S. J.; Kim, T.; Jung, B. M.; Lee, S. B.; Park, B. Absorption-dominant, low reflection EMI shielding materials with integrated metal mesh/TPU/CIP composite. *Chem. Eng. J.* **2022**, *428*, 131167.
[171] Ryu, S. H.; Kim, H.; Park, S. W.; Kwon, S. J.; Kim, S.; Lim, H. R.; Park, B.; Lee, S. B.; Choa, Y. H. Millimeter-scale percolated polyethylene/graphene composites for 5G electromagnetic shielding. *ACS Appl. Nano Mater.* **2022**, *5*, 8429–8439.
[172] Lin, Z. H.; Liu, J.; Peng, W.; Zhu, Y. Y.; Zhao, Y.; Jiang, K.; Peng, M.; Tan, Y. W. Highly stable 3D $Ti_3C_2T_x$ MXene-based foam architectures toward high-performance terahertz radiation shielding. *ACS Nano* **2020**, *14*, 2109–2117.